

THE X-RAY POLARIZATION SIGNATURE OF QUIESCENT MAGNETARS: EFFECT OF MAGNETOSPHERIC SCATTERING AND VACUUM POLARIZATION

RODRIGO FERNÁNDEZ^{1,2} AND SHANE W. DAVIS^{1,3}

Draft version October 8, 2018

ABSTRACT

In the magnetar model, the quiescent non-thermal soft X-ray emission from Anomalous X-ray Pulsars and Soft-Gamma Repeaters is thought to arise from resonant comptonization of thermal photons by charges moving in a twisted magnetosphere. Robust inference of physical quantities from observations is difficult, because the process depends strongly on geometry and current understanding of the magnetosphere is not very deep. The polarization of soft X-ray photons is an independent source of information, and its magnetospheric imprint remains only partially explored. In this paper we calculate how resonant cyclotron scattering would modify the observed polarization signal relative to the surface emission, using a multidimensional Monte Carlo radiative transfer code that accounts for the gradual coupling of polarization eigenmodes as photons leave the magnetosphere. We employ a globally-twisted, self-similar, force-free magnetosphere with a power-law momentum distribution, assume a blackbody spectrum for the seed photons, account for general relativistic light deflection close to the star, and assume that vacuum polarization dominates the dielectric properties of the magnetosphere. The latter is a good approximation if the pair multiplicity is not much larger than unity. Phase-averaged polarimetry is able to provide a clear signature of the magnetospheric reprocessing of thermal photons and to constrain mechanisms generating the thermal emission. Phase-resolved polarimetry, in addition, can characterize the spatial extent and magnitude of the magnetospheric twist angle at ~ 100 stellar radii, and discern between uni- or bidirectional particle energy distributions, almost independently of every other parameter in the system. We discuss prospects for detectability with GEMS.

Subject headings: radiative transfer — magnetic fields — plasmas — stars: neutron — X-rays: stars — techniques: polarimetric

1. INTRODUCTION

The rich phenomenology associated with Soft Gamma Repeaters (SGRs; e.g. Mereghetti et al. 2007) and Anomalous X-ray Pulsars (AXPs; e.g. Kaspi 2007) has so far been best accounted for by the *magnetar* model, which hypothesizes the decay of a strong magnetic field in a neutron star as the dominant energy source (Duncan & Thompson 1992; Thompson & Duncan 1996).

In the soft X-ray band (1–10 keV), the quiescent spectra of magnetar candidates are, to first approximation, very similar: a thermal component with temperature $kT \sim 0.4$ keV, and a non-thermal tail of varying hardness at higher energies (e.g., Woods & Thompson 2006). On an individual basis, though, quiescent AXPs and SGRs can show variability in their spectra and pulse profiles over timescales ranging from days to years, in many cases around outburst periods or glitches (e.g., Kaspi 2007; Woods et al. 2007).

In the magnetar model, the non-thermal component of the spectrum arises from the decay of the toroidal part of the magnetospheric field (the “twist”), thought to be acquired during outbursts (Thompson et al. 2002). The twist induces a current along the field lines, increasing the density of charges by orders of magnitude above the Goldreich & Julian (1969) value, resulting in an optical depth to resonant cyclotron scattering of order unity. Comptonization of thermal photons from the stellar surface then generates a non-thermal tail in the spectrum, and pulsed emission from the combination of stellar rotation and the geometric dependence of the process (Thompson et al.

2002).

Numerical calculations of the resulting emission have been carried out with both one-dimensional semianalytic methods (Lyutikov & Gavril 2006) and multidimensional Monte Carlo algorithms (Fernández & Thompson 2007; Nobili et al. 2008). Output from the one-dimensional computation has been used to model phase averaged spectra of AXPs and SGRs (Güver et al. 2007, 2008; Rea et al. 2007a, 2008), resulting in good fits while improving upon the ad-hoc blackbody plus power-law prescription. Even better fits are obtained when using the results of the Nobili et al. (2008) calculation, as no extra power-law is required to fit SGR spectra (Zane et al. 2009).

Still, phase averaged observables convey only part of the information, raising the question of geometric degeneracies. Recently, Albano et al. (2010) have performed simultaneous light curve and spectral fitting of the transient AXPs XTE J1810-197 and CXOU J164710.2-455216, making use of the Nobili et al. (2008) output, constraining for the first time the geometric orientation of these sources and hence providing a more robust spectral fit. Nevertheless, both the Fernández & Thompson (2007) and Nobili et al. (2008) studies make reasonable but heuristic assumptions about the magnetospheric physics, caused largely by the difficulty of modeling the closed field line circuit with radiation feedback from first principles.

Barring an improved understanding of the physics, further progress is possible by making use of information encoded in the polarization signal. In recent years, photoelectric polarimeters have reached the sensitivity level required for detecting polarized X-rays from a variety of astrophysical sources (Costa et al. 2001; Black et al. 2007), allowing extension of the discovery space beyond the lone data point for the Crab nebula (Novick et al. 1972). In particular, the Gravity

¹ Institute for Advanced Study, Einstein Drive, Princeton, NJ 08540, USA.

² Einstein Fellow

³ Canadian Institute for Theoretical Astrophysics, Toronto, ON M5S3H4, Canada.

and Extreme Magnetism (GEMS) mission will reach a Minimum Detectable Polarization (MDP) of $\sim 1\%$ for a 1 mCrab source in the 2–10 keV range with a 10^6 s integration (Swank et al. 2010). About one half of the current magnetar candidates are brighter than 1 mCrab⁴, making detection of their polarization a concrete possibility.

Polarized X-ray transfer calculations have been carried out for isolated neutron stars with dipole-type magnetic fields, in some cases including realistic atmospheres but with no magnetospheric processes other than propagation in a Schwarzschild spacetime (Heyl & Shaviv 2000; Pavlov & Zavlin 2000; Heyl et al. 2003; van Adelsberg & Lai 2006; Wang & Lai 2007; van Adelsberg & Perna 2009; Wang & Lai 2009). Both the Fernández & Thompson (2007) and Nobili et al. (2008) Monte Carlo studies assume adiabatic propagation, with photons remaining in a fixed polarization eigenmode in between scatterings, until they escape the magnetosphere. Nobili et al. (2008) estimated the observed polarization fractions through the relative difference between the emerging normal mode intensities. The polarization measured by a distant observer, however, is set by a gradual coupling of the propagation eigenmodes as photons leave the magnetosphere, with the generation of a circular component in some cases (Heyl & Shaviv 2000). Thus, evolution of all polarization degrees of freedom is required for making observational predictions.

In this paper we extend the multidimensional Monte Carlo radiative transfer code of Fernández & Thompson (2007) to include polarization propagation and general relativistic light deflection close to the neutron star. Our focus is to understand the basic features imparted to the polarization signal by the scattering process and the geometry of the system. To this end, we perform radiative transfer simulations using the simplest possible prescriptions for magnetic field geometry, particle energy distribution, and seed photons, when the dielectric properties of the medium are dominated by vacuum polarization. Motivated by GEMS, we explore the parameter dependencies of polarization fraction and polarization angle.

The structure of this paper is the following. Section 2 lays out the physics included in the model, while Section 3 discusses our numerical implementation. Section 4 contains our results, focusing on the dependence of observables on system parameters. In Section 5 we discuss our findings in light of the expected instrumental parameters of GEMS, and estimate integration times for a few bright magnetar candidates. A summary and discussion of our results is provided in Section 6; readers not interested in technical details can start here, where explicit reference is made to the key figures and equations. Appendix A contains details about geometric transformations employed in the code.

2. PHYSICAL MODEL

The elements influencing the polarization signal measured at infinity are: (i) the physics of the magnetosphere, including the transfer of polarized radiation, (ii) the properties of the seed photons, and (iii) the type of spacetime. We describe our treatment of each of these items in turn. A detailed description of the physics entering the twisted magnetosphere model can be found in Thompson et al. (2002) and Fernández & Thompson (2007). Here we provide a minimal account, focused on the part relevant to polarization observables.

2.1. Twisted Magnetosphere

The basic hypothesis behind the magnetar model is the existence of a strong toroidal field inside the star, thought to have been generated via dynamo action in a rapidly rotating protoneutron star (Thompson & Duncan 1995; Thompson & Duncan 2001). Seismic instabilities in the crust induced by strong magnetic stresses mediate the transfer of some of this internal toroidal energy to the magnetosphere, imparting a finite twist to the otherwise dipolar external field (Thompson & Duncan 2001; Thompson et al. 2002; Beloborodov & Thompson 2007).

To describe such a magnetosphere, one would ideally solve a closed field line circuit including pair creation processes and feedback from radiation at cyclotron frequencies (e.g., Thompson et al. 2002; Beloborodov & Thompson 2007; Thompson 2008a,b). The global problem has not yet been solved self-consistently. Numerical computations of the X-ray emission rely instead on prescriptions for the field geometry and particle energy distribution that can capture the basic aspects of the model (Fernández & Thompson 2007; Nobili et al. 2008; Pavan et al. 2009). As our goal here is to explore the dependence of the polarization signal on different parameters rather than to fit individual sources, we adopt the same parametric approach in our calculations.

2.1.1. Magnetic Field Geometry and Particle Energy Distribution

We adopt the force-free, self-similar, twisted-dipole solution of Thompson et al. (2002),

$$\mathbf{B} = \frac{1}{2} B_{\text{pole}} \left(\frac{R_{\text{NS}}}{r} \right)^{2+p} \mathbf{F}(\cos \theta), \quad (1)$$

with r the radial distance from the center of the star, θ the polar angle relative to the magnetic axis, B_{pole} the strength of the field at the poles, R_{NS} the stellar radius, and p a constant. The components of the function \mathbf{F} are $F_r = -f'$, $F_\theta = (p/\sin \theta)f$, and $F_\phi = [C/\{p(p+1)\}]f^{1/p}F_\theta$, with $f(\cos \theta)$ the solution to the second order differential equation

$$\sin^2 \theta f'' + C f^{1+2/p} + p(p+1)f = 0, \quad (2)$$

subject to the boundary conditions $f'(0) = 0$, $f'(1) = -2$, and $f(1) = 0$. This leaves an additional free parameter, either C or p . Alternatively, one can label solutions by the net twist angle of the field lines that are anchored close to the magnetic poles,

$$\Delta \phi_{N-S} = 2 \lim_{\theta_0 \rightarrow 0} \int_{\theta_0}^{\pi/2} \frac{B_\phi}{B_\theta} \frac{d\theta}{\sin \theta}. \quad (3)$$

When going from $\Delta \phi_{N-S} = 0$ to π , the solutions interpolate smoothly between a dipole ($p = 1$) and a split monopole ($p = 0$). For illustration, Figure 1 shows a few field lines anchored at 15° from the magnetic axis for a twist $\Delta \phi_{N-S} = 1$.

The current density induced along the twisted lines is (Thompson et al. 2002)

$$\mathbf{J} = \sum_i Z_i e n_i \bar{\beta}_i \hat{\mathbf{B}} c = \frac{(p+1)c}{4\pi r} \frac{B_\phi}{B_\theta} \mathbf{B}, \quad (4)$$

where $Z_i e$ is the electric charge of species i , n_i the number density, $\hat{\mathbf{B}} = \mathbf{B}/B$, and

$$\bar{\beta}_i = \int f_i(\mathbf{r}, p) \frac{pc}{E} dp \quad (5)$$

⁴ A catalog of current magnetar candidates is maintained at <http://www.physics.mcgill.ca/~pulsar/magnetar/main.html>

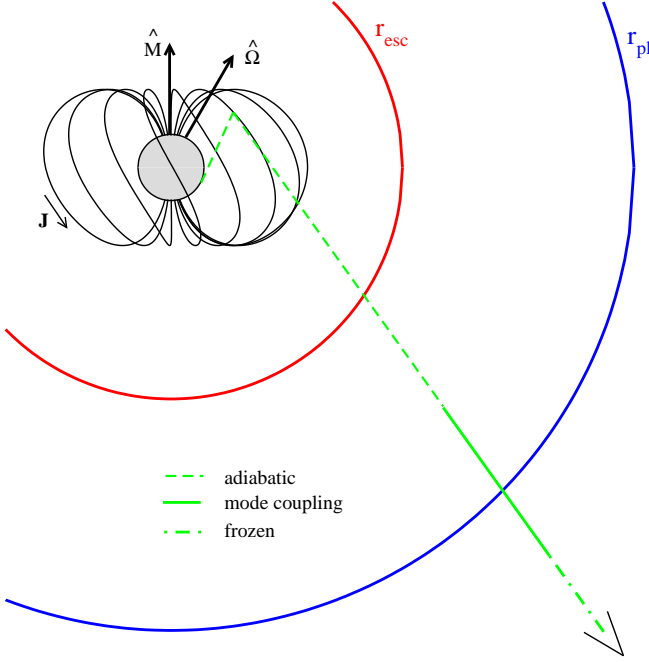


FIG. 1.— Diagram showing the spatial arrangement of the problem (not to scale). The neutron star (grey circle) emits thermal photons (green trajectory) which scatter electrons moving along field lines (black solid lines). Magnetospheric charges are provided by a current \mathbf{J} due to the net magnetospheric twist (§2.1.1). Photons can scatter only inside r_{esc} (eq. [26]). At radii much smaller than r_{pl} (eq. [27]), the polarization propagation is adiabatic (dashed green line, §2.1.3). When approaching this radius, polarization eigenmodes start to couple (solid green) and eventually freeze beyond r_{pl} (dot-dashed green). For clarity, only a few field lines anchored at 15° from the magnetic axis are shown, for a twist angle $\Delta\phi_{\text{N-S}} = 1$ (eq. [3]). Photon trajectories are curved close to the star due to light-bending (§2.3). The vectors $\hat{\mathbf{M}}$ and $\hat{\boldsymbol{\Omega}}$ denote the magnetic and rotation axes, respectively.

the mean velocity along the field lines in units of c , with $f(\mathbf{r}, p)$ the one-dimensional phase-space distribution function, normalized such that $\int f(\mathbf{r}, p) dp = 1$. The number density of charges n_i is obtained from

$$\frac{|Z_i|en_i}{B} = \epsilon_i \frac{(p+1) B_\phi}{4\pi r \beta_i B_\theta}, \quad (6)$$

where ϵ_i is the fraction of the current carried by species i .

To complete the description of the magnetosphere one needs to specify the particle energy distribution of the charge carriers. We employ the simplest possible prescription, a power law in momentum, independent of position,

$$f(\gamma\beta) \propto (\gamma\beta)^{-\alpha}, \quad (7)$$

where $\gamma = (1 - \beta^2)^{-1/2}$ is the Lorentz factor. This distribution is characterized by three parameters: the exponent α , the minimum velocity β_{min} , and the maximum Lorentz factor γ_{max} . In all of our runs we employ $\alpha = -2$ and $\beta_{\text{min}} = 0.2$, but allow γ_{max} to vary (see, e.g., Fernández & Thompson 2007 for the resulting spectra and their comparison with other distribution functions). To account for both an electron-ion and electron-positron plasma in the magnetosphere, we allow equation (7) to be uni- or bi-directional, that is, extending over only positive (from north to south magnetic pole, Fig. [1]) or both positive and negative momenta⁵.

⁵ In the case of an electron-ion plasma, the relevant charge carrier for the interaction with keV X-rays far from the star are only the electrons.

In the simple case considered here ($n_e \sim J/[ec]$), the dielectric and inverse permeability tensors are dominated by vacuum polarization (§2.1.3). As a first step in addressing this problem, and to ease comparison with previous work, we ignore the possibility of a large pair multiplicity, in which case $n_e \gg J/[ec]$. Such an effect could result from pair cascades originated by the energy deposition of current-driven instabilities and the rapid conversion of resonantly upscattered X-rays into pairs under a strong magnetic field (Thompson 2008a). This could significantly modify the dielectric properties at distances from the star where the adiabatic approximation breaks down. Given that our modeling of the magnetospheric currents is rather heuristic, the inclusion of plasma polarization could lead to artificial features sensitive to the temperature and density of the magnetospheric particles. Hence, we opt for a self-consistent but potentially incomplete calculation, and only include vacuum polarization. Consequently, we set $\epsilon_i \equiv \epsilon = 1$ in equation (6) for an ion-electron plasma, or $\epsilon_i = 1/2$ when electrons and positrons are present.

2.1.2. Resonant Cyclotron Scattering

For magnetar field strengths, the lifetime of an excited Landau level is very short, $\Delta t_L = (3/4)(\hbar/[\alpha_{\text{em}} m_e c^2])(B_{\text{QED}}/B)^2 \simeq 3 \times 10^{-14} B_{11}^{-2}$ s, with α_{em} the fine structure constant, $B_{\text{QED}} = m_e^2 c^3 / (\hbar e) \simeq 4.4 \times 10^{13}$ G the field strength where the cyclotron energy equals the electron rest mass energy, and $B_{11} \equiv B/(10^{11} \text{G})$. Hence, electrons or positrons can be assumed to be in the ground state, and absorption plus re-emission of photons can be treated as a single scattering process (Zheleznyakov 1996). Excitation occurs when the photon frequency, in the rest frame of the charge, equals the cyclotron frequency. In the stellar frame, this condition corresponds to

$$\omega = \omega_D \equiv \frac{\omega_c}{\gamma(1 - \beta\mu)}, \quad (8)$$

where ω is the photon angular frequency,

$$\mu = \hat{\mathbf{k}} \cdot \hat{\mathbf{B}} \quad (9)$$

is the cosine of the angle between photon ($\hat{\mathbf{k}}$) and magnetic field directions in the *stellar frame*, and

$$\omega_c = \frac{eB}{m_e c} \simeq 1.2 B_{11} \frac{\text{keV}}{\hbar} \quad (10)$$

the electron cyclotron frequency.

The total cross section in the stellar frame is given by (e.g., Mészáros 1992)

$$\sigma_{\text{res}} = 4\pi^2 (1 - \beta\mu) \frac{|Z|e}{B} |e_\pm|^2 \omega_D \delta(\omega - \omega_D), \quad (11)$$

where $|e_\pm|$ is the *rest frame* overlap of the photon polarization state with a left (-) or right (+) circularly polarized wave, depending on the sign of the charge. The factor $(1 - \beta\mu)$ comes from the relativistic boost to the cross section (e.g., Rybicki & Lightman 2004). The delta function is an approximation to the small fractional width of the resonance for a single particle, $(2\Delta t_L \omega_c)^{-1} = (2\alpha_{\text{em}}/3)(B/B_{\text{QED}}) = 10^{-5} B_{11}$. The enhancement relative to the usual non-resonant Thomson cross section σ_T is, at resonance and in the charge rest frame, $\sigma_{\text{res}}/\sigma_T = |e_\pm|^2 (2\Delta t_L \omega_c)^2 \sim 10^{10} |e_\pm|^2 B_{11}^2$ (Mészáros 1992).

Calculation of the optical depth requires averaging the cross section over the phase space distribution of the scattering charges. Using the fact that for fixed photon frequency and

at a given position, equation (8) has two roots β^\pm , the differential optical depth along a small distance $\Delta\ell \ll r$ is given by (Fernández & Thompson 2007)

$$\Delta\bar{\tau}_{\text{res}} = \varepsilon \frac{\pi(p+1)\omega}{r|\beta|} \left(\frac{B_\phi}{B_\theta} \right) \left[(1-\beta^+\mu)|e_\pm|_{\gamma\beta^+}^2 \frac{f(\gamma\beta^+)\Delta(\gamma\beta^+)}{(\partial\omega_D/\partial\ell)_{\gamma\beta^+}} - (1-\beta^-\mu)|e_\pm|_{\gamma\beta^-}^2 \frac{f(\gamma\beta^-)\Delta(\gamma\beta^-)}{(\partial\omega_D/\partial\ell)_{\gamma\beta^-}} \right], \quad (12)$$

where $(\gamma\beta)^\pm$ are the resonant momenta corresponding to the resonant velocities β^\pm , $\Delta(\gamma\beta)^\pm$ is the size of the step in resonant-momentum space corresponding to the spatial step $\Delta\ell$, and $\partial\omega_D/\partial\ell = \hat{k} \cdot \nabla\omega_D$. Equation (12) differs from Fernández & Thompson (2007) in that the average velocity $|\beta|$ comes out of the integral, as it is given by the relation between current density and number density (eq. [4]) and does not depend on the resonance condition⁶. Given that typical values of β are not too far from the mean of the distribution, this modification does not introduce a significant difference in the results relative to those of Fernández & Thompson (2007).

During scattering, a photon can change its polarization state. The probabilities depend on the rest frame overlap of the outgoing photon polarization with a circularly polarized wave, as the differential cross section for scattering from polarization state A to state B satisfies (Mészáros 1992)

$$\frac{d\sigma_{\text{res}}}{d\Omega'} \propto |e_\pm|_A^2 |e'_\pm|_B^2, \quad (13)$$

where primes denote outgoing photon quantities. If normal modes begin to couple, the simple adiabatic expressions for the *ingoing* photon overlap need to be modified, as described in §3.2 (eq. [33]). For the *outgoing* photon, however, we impose a normal mode state, regardless of the degree of adiabaticity. As vacuum polarization dominates the dielectric properties (§2.1.3), the electric field eigenvectors are given by $\hat{e}_E \propto (\hat{k} \times \hat{B})$ and $\hat{e}_O \propto (\hat{e}_E \times \hat{k})$. The overlap is the dot product of the normalized eigenvectors with $\hat{e}_\pm = (\hat{x} \pm i\hat{y})/\sqrt{2}$ in a frame where \hat{B} is along \hat{z} , yielding

$$|e'_\pm|_E^2 = 1/2, \quad |e'_\pm|_O^2 = (\mu'_r)^2/2, \quad (14)$$

where

$$\mu_r = \frac{\mu - \beta}{1 - \beta\mu} \quad (15)$$

is the angle between photon direction and magnetic field in the *rest frame* of the charge. The probability of the photon coming out in E-mode is then

$$P(E) = \frac{1}{1 + (\mu'_r)^2}, \quad (16)$$

with $P(O) = 1 - P(E)$. In practice, imposing a normal mode right after scattering does not affect our results, as the polarization coupling and scattering regions are well separated in space (§2.1.3, see also Figure 2).

Note that for all $|\mu'_r| < 1$, $P(O) < P(E)$, and hence E-mode photons always dominate the outgoing polarization distribution except for exactly parallel propagation.

⁶ Nobili et al. (2008) used an optical depth with this error corrected. The factor $\omega_D^{-1}(\partial\omega_D/\partial\ell)$ is independent of $\omega_D = \omega$, so there is no dependence on photon frequency or magnetic field strength.

2.1.3. Transfer of Polarized Radiation

We first analyze the dielectric properties of the magnetosphere, then write down the polarization evolution equations, and finally characterize the regions over which magnetospheric scattering and non-adiabatic propagation are relevant, looking for possible overlaps.

For $B \ll B_{\text{QED}}$, the relative contributions of plasma and vacuum polarization to the dielectric and inverse permeability tensors can be quantified by the ratio (e.g., Zheleznyakov 1996)

$$\frac{(\omega_p/\omega)^2/|\beta|}{\alpha_{\text{em}}(B/B_{\text{QED}})^2/45\pi} \simeq 10^{-7} B_{\text{pole},14}^{-1} R_6^{-1} \left(\frac{r}{R_{\text{NS}}} \right)^{1+p} \times \frac{\sin^2\theta \Delta\phi_{\text{N-S}}}{|\beta|} \left(\frac{\hbar\omega}{\text{keV}} \right)^{-2}, \quad (17)$$

where $\omega_p = \sqrt{4\pi Z^2 e^2 n_e/m_e}$ is the electron plasma frequency, and the current density (eq. [4]) has been approximated by $\mathbf{J} \simeq c(4\pi r)^{-1} \sin^2\theta \Delta\phi_{\text{N-S}} \mathbf{B}$ (Thompson et al. 2002). Equation (17) shows that vacuum polarization dominates out to $r \simeq 3000 R_{\text{NS}}$ for mildly relativistic particle distributions ($|\beta| \lesssim 1$). Outside this radius plasma polarization starts to dominate.

We show in §3.3 that the polarization vector effectively freezes at distances $\lesssim 500 R_{\text{NS}}$, well inside the vacuum dominated regime. However, this would change if the pair multiplicity is bigger than $\mathcal{M}_\pm \sim 10^3$, because the radius where plasma and vacuum polarization become comparable would decrease by a factor $(\mathcal{M}_\pm)^{1/(1+p)} \sim 30$.

Due to quantum electrodynamic effects, a strong magnetic field modifies the dielectric properties of the vacuum according to (Klein & Nigam 1964; Adler 1971)

$$\varepsilon = (1+a)\mathbb{I} + q\hat{B}\hat{B} \quad (18)$$

$$\bar{\mu} = (1+a)\mathbb{I} + m\hat{B}\hat{B}, \quad (19)$$

where ε and $\bar{\mu}$ are the dielectric and inverse permeability tensors, respectively, and \mathbb{I} is the unit tensor. For $B \ll B_{\text{QED}}$, the coefficients are $a = -2\delta$, $q = 7\delta$, and $m = -4\delta$, with $\delta = \alpha_{\text{em}}(45\pi)^{-1}(B/B_{\text{QED}})^2 \simeq 3 \times 10^{-10} B_{11}^2$. These coefficients are all real, so there is no change in the total intensity. The propagation eigenmodes are linear, and are defined in relation to the photon and magnetic field directions (§2.1.2). General expressions exist for arbitrary field strengths, which nevertheless maintain the geometric structure of equations (18)-(19) [Heyl & Hernquist 1997]. Given that polarization eigenmodes begin to decouple at distances $r \gtrsim 10 R_{\text{NS}}$, the weak field limit is good enough for our purposes.

The polarization of photons can be characterized through the complex components of the electric field vector in some coordinate system, or through the Stokes parameters (e.g., Rybicki & Lightman 2004). In our implementation, we choose to evolve the former, as it is simpler to perform geometric transformations on them, and convert to Stokes parameters only after the polarization is deemed to be frozen (§3.3).

We now derive the ordinary differential equations governing the evolution of the electric field vector in the geometric optics limit, following the notation of Lai & Ho (2003b). The wave equation for the electric field of a plane electromagnetic wave $\mathbf{E} = \mathbf{E}_0(\mathbf{r})e^{-i\omega t}$ is

$$\nabla \times [\bar{\mu} \cdot (\nabla \times \mathbf{E})] = \frac{\omega^2}{c^2} \varepsilon \cdot \mathbf{E}. \quad (20)$$

The polarization tensors are assumed to be constant in time and varying over distances much larger than the photon wavelength. We then choose a coordinate system with the z -axis along the direction of photon propagation, assume that quantities change only along z , and write $\mathbf{E}_0(z) = \exp(ik_0 z) \mathbf{A}(z)$, with $k_0 = \omega/c$. The geometric optics approximation is equivalent to $\partial_z \mathbf{A} \ll k_0 \mathbf{A}$. Keeping terms linear in $k_0^{-1} \partial_z$, we obtain a system of ordinary differential equations describing the propagation of the complex amplitude \mathbf{A} ,

$$\partial_z A_x = \frac{ik_0}{2} \left(\bar{\mu}_{yy} - \frac{\bar{\mu}_{xy}\bar{\mu}_{yx}}{\bar{\mu}_{xx}} \right)^{-1} \left[\left(\varepsilon_{xx} - \bar{\mu}_{yy} + \frac{\bar{\mu}_{yx}}{\bar{\mu}_{xx}} [\varepsilon_{yx} + \bar{\mu}_{xy}] \right) A_x + \left(\varepsilon_{xy} + \bar{\mu}_{yx} + \frac{\bar{\mu}_{yx}}{\bar{\mu}_{xx}} [\varepsilon_{yy} - \bar{\mu}_{xx}] \right) A_y \right] \quad (21)$$

$$\partial_z A_y = \frac{ik_0}{2} \left(\bar{\mu}_{xx} - \frac{\bar{\mu}_{xy}\bar{\mu}_{yx}}{\bar{\mu}_{yy}} \right)^{-1} \left[\left(\varepsilon_{xy} + \bar{\mu}_{yx} + \frac{\bar{\mu}_{yx}}{\bar{\mu}_{yy}} [\varepsilon_{xx} - \bar{\mu}_{yy}] \right) A_x + \left(\varepsilon_{yy} - \bar{\mu}_{xx} + \frac{\bar{\mu}_{yx}}{\bar{\mu}_{yy}} [\varepsilon_{xy} + \bar{\mu}_{yx}] \right) A_y \right] \quad (22)$$

$$A_z = -\frac{\varepsilon_{zx}}{\varepsilon_{zz}} A_x - \frac{\varepsilon_{zy}}{\varepsilon_{zz}} A_y. \quad (23)$$

Equations (21)-(23) are valid for general conditions, so long as the geometric optics and smooth background approximation holds. Inclusion of the plasma contribution to $\bar{\mu}$ and ε is mathematically straightforward, once the number density and temperature of charges as a function of position are known (see, e.g., Lai & Ho 2003b for an application to neutron star atmospheres).

Even for magnetar field strengths, the non-diagonal components of ε are much smaller than unity, hence from equation (23) we can neglect A_z . To more clearly visualize the behavior of equations (21)-(22), one can switch to a reference frame where the magnetic field is in the x - z plane, $\hat{B} = \cos \theta_{kB} \hat{k} + \sin \theta_{kB} \hat{x}$, and keep terms linear in $\{a, q, m\}$, finding

$$\frac{\partial}{\partial z} \begin{pmatrix} A_x \\ A_y \end{pmatrix} = \frac{i}{2} k_0 \sin^2 \theta_{kB} \begin{pmatrix} q & 0 \\ 0 & -m \end{pmatrix} \begin{pmatrix} A_x \\ A_y \end{pmatrix}. \quad (24)$$

In this case, the x and y components correspond to the O- and E-mode eigenvectors, respectively. The characteristic scale over which \mathbf{A} varies is

$$\ell_A = \frac{1}{k_0 \Delta n}, \quad (25)$$

where $\Delta n = \sin^2 \theta_{kB} (q + m)/2$ is the difference between the indices of refraction (Heyl & Shaviv 2000; Lai & Ho 2003b). As the photon propagates, non-diagonal components will appear in equation (24), because \hat{B} will leave the x - z plane. However, if this occurs over a length-scale much larger than ℓ_A , normal modes do not mix, and the propagation is *adiabatic* (Heyl & Shaviv 2000; Lai & Ho 2003b). As the photon moves out in the magnetosphere, the QED correction to the dielectric tensor falls off as $B^2 \sim r^{-6}$, causing ℓ_A to increase in magnitude, until the point at which the polarization effectively freezes. The distance from the star at which the adiabatic approximation breaks down is usually called the *polarization limiting radius* (Heyl et al. 2003), and is given by the radius at which the relation $B/|\hat{k} \cdot \nabla B| \sim \ell_A$ is satisfied (see Heyl et al. 2003; Lai & Ho 2003b for slightly different criteria). The coupling of the modes is gradual, however, and a characterization of the observed polarization signal requires solution of equations (21)-(22) over this coupling region.

It is instructive to quantify the size of the regions where resonant scattering and mode coupling are relevant, as this determines the simplifications that are possible in the full problem. The surface inside which resonant cyclotron scattering can occur is the *escape radius*, given by the condition $(\omega_c/\omega)^2 + \mu^2 = 1$ (Fernández & Thompson 2007). Outside of this surface, there is no particle velocity such that the resonance condition (eq. [8]) can be satisfied. For the twisted dipole geometry, it is given by

$$\begin{aligned} r_{\text{esc}} &= r_{\text{esc}}(\theta, \omega, \hat{k}, B_{\text{pole}}, \Delta\phi_{N-S}, R_{\text{NS}}) \\ &= \left[\xi (1 - \mu^2)^{-1/2} \left(\frac{\omega_{c,\text{pole}}}{\omega} \right) \right]^{1/(2+p)} R_{\text{NS}} \\ &\simeq 12 \left[\xi (1 - \mu^2)^{-1/2} B_{\text{pole},14} \left(\frac{\text{keV}}{\hbar\omega} \right) \right]_{\Delta\phi=1}^{1/2.88} R_{\text{NS}}, \end{aligned} \quad (26)$$

where $\omega_{c,\text{pole}} = eB_{\text{pole}}/(m_e c)$, and $2\xi = [\mathbf{F}^2(\cos \theta)]^{1/2}$ is the angular dependence of the magnetic field strength (c.f. eq. [1]). The polarization limiting radius is set by the equality between ℓ_A and the length scale over which the field strength changes, $\ell_B = B/|\hat{k} \cdot \nabla B|$. Writing $\ell_B = r/\zeta(\theta, \hat{k}, \Delta\phi_{N-S})$, where ζ is a dimensionless function of order unity, we find

$$\begin{aligned} r_{\text{pl}} &= r_{\text{pl}}(\theta, \omega, \hat{k}, B_{\text{pole}}, \Delta\phi_{N-S}, R_{\text{NS}}) \\ &= R_{\text{NS}} \left[\left(\frac{\alpha_{\text{em}}}{30\pi} \right) \left(\frac{B_{\text{pole}}}{B_{\text{QED}}} \right)^2 (1 - \mu^2) \frac{\xi^2}{\zeta} \left(\frac{R_{\text{NS}} \omega}{c} \right) \right]^{1/(3+2p)} \end{aligned} \quad (27)$$

$$\simeq 146 \left[(1 - \mu^2) \frac{\xi^2}{\zeta} B_{\text{pole},14}^2 R_6 \left(\frac{\hbar\omega}{\text{keV}} \right) \right]_{\Delta\phi=1}^{1/4.76} R_{\text{NS}}, \quad (28)$$

where $R_6 = R_{\text{NS}}/10^6$ cm.

Figure 2 shows r_{esc} and r_{pl} as a function of photon direction angles, for 1 keV photons at the magnetic equator, with a twist $\Delta\phi_{\text{NS}} = 1$ and a standard choice for other parameters. Aside from narrow regions where the surfaces become singular ($|\mu| \rightarrow 1$ for r_{esc} and $\hat{k} \cdot \nabla B \rightarrow 0$ for r_{pl}), they are well separated by an order of magnitude in radius. Photons in the Rayleigh-Jeans tail of the thermal spectrum could in principle violate this separation, but they contribute little to the observed signal. One can thus assume that (1) scattering is largely decoupled from polarization evolution, taking place mostly within the adiabatic propagation region, and (2) the polarization signal is set at distances $\gtrsim 100 R_{\text{NS}}$ from the center, where the effects of general relativity are weak.

2.2. Seed Photon Distribution

Two physical processes have been proposed to explain the thermal component of the quiescent soft X-ray spectrum. The first is heat generated in the core by ambipolar diffusion (Thompson & Duncan 1996). These photons are expected to emerge in E-mode polarization, as their free-free opacity is suppressed relative to the O-mode (e.g., Lai & Ho 2002). Including resonant mode conversion at magnetar field strengths ($\gtrsim 10^{14}$ G at the surface) does not alter this dominance of the E-mode, but instead modifies the spectral shape (e.g., Lai & Ho 2003a). For the purposes of exploring the effects of magnetospheric scattering on the surface polarization, we adopt a simple blackbody spectrum with a temperature such that its value measured at infinity is $kT = 0.4$ keV. This case is assigned a 100% initial polarization in the E-mode.

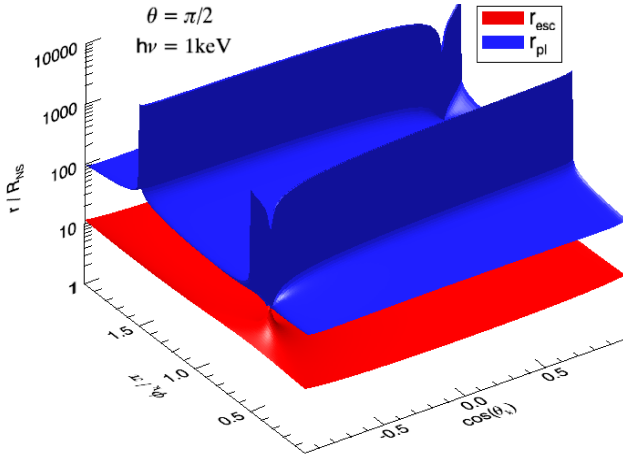


FIG. 2.— Escape radius r_{esc} (eq. [26], red surface) and polarization limiting radius r_{pl} (eq. [27], blue surface) for 1 keV photons at the magnetic equator, as a function of photon direction $\hat{k}(\theta_k, \phi_k)$, with θ_k and ϕ_k the polar and azimuthal angle of \hat{k} relative to the magnetic axis, respectively. Other parameters are $B_{\text{pole}} = 10^{14}$ G, $\Delta\phi_{\text{NS}} = 1$ rad, and $R_{\text{NS}} = 10^6$ cm. The spikes in the surfaces arise at points where the expressions become singular, namely $|\mu| \rightarrow 1$ for r_{esc} and $\hat{k} \cdot \nabla B \rightarrow 0$ for r_{pl} .

The second source of thermal photons is the deposition of energy at the stellar surface by *returning currents* in a layer that is optically thick to free-free absorption (Thompson et al. 2002; Beloborodov & Thompson 2007). In this case, the emission is expected to emerge predominantly in O-mode polarization. Since the details of this mechanism have not been thoroughly explored yet, we account for this possibility by simply changing the outgoing polarization distribution from E- to O-mode. Intermediate mixtures (such as a completely unpolarized case) can be obtained by linear superposition.

Regardless of the mechanism responsible for the seed photons, emission is expected to be anisotropic over the stellar surface. For the deep cooling case, even a constant temperature atmosphere has an emerging radiation intensity that is beamed relative to the magnetic field direction, with an angular distribution that depends on photon energy and magnetic field strength (van Adelsberg & Lai 2006). Additional anisotropies are expected due to the suppression of thermal conduction across magnetic field lines. If a strong internal toroidal field is present, very narrow polar caps are expected (Pérez-Azorín et al. 2006; Geppert et al. 2006). If the thermal emission is powered by returning currents, localized hot spots of the size of the current carrying region would be natural. We explore the effects of anisotropies in the surface temperature by running additional models restricting emission to polar caps with a size of 5 degrees. We do not attempt here to include the effect of beaming of radiation around the local magnetic field direction. It is worth keeping in mind, though, that general relativistic deflection of photon trajectories significantly smears out emission from a polar cap, enlarging its apparent angular size (§2.3).

2.3. Spacetime Properties

Magnetars are slow rotators, with periods falling in the range 2–10 s (e.g., Woods & Thompson 2006). At the surface of the star, corrections to the metric due to rotation are of order $(J_{\text{NS}}/[M_{\text{NS}}R_{\text{NS}}c])^2 \sim (R_{\text{NS}}\Omega/c)^2 \lesssim 4 \times 10^{-8} R_6^2 P_{\text{sec}}^{-2}$, where J_{NS} , M_{NS} , and $\Omega = 2\pi/P$ are the stellar angular momentum,

mass, and angular velocity, respectively, and $P_{\text{sec}} = P/1$ s. Hence, using a Schwarzschild spacetime is a very good approximation.

In §2.1.3 we showed that the polarization signal is determined at radii $\gtrsim 100R_{\text{NS}}$, where the effects of general relativity on photon propagation are weak. However, a significant fraction of the seed photons leaves the magnetosphere without scattering, thus inclusion of light-bending is needed to properly account for the fraction of the stellar surface contributing to the unscattered polarization signal. This is particularly important when including emission from hot spots, as bending angles are as large as 30 degrees for typical neutron star parameters (e.g., Beloborodov 2002).

We adopt the approach of Heyl et al. (2003) for inclusion of general relativity in our polarization calculation. That is, (1) modifications to the magnetic field are ignored, as close to the star this is of weak importance for both scattering and polarization⁷; (2) the polarization plane is parallel transported along photon geodesics; and (3) we ignore general relativistic corrections to the polarization transfer equations (21–22) other than the modification of the polarization plane.

3. NUMERICAL IMPLEMENTATION

Our Monte Carlo code has been extensively described in Fernández & Thompson (2007). We describe here the modifications introduced in the present study.

3.1. Propagation

Integration of photon trajectories in a Schwarzschild metric is a standard textbook calculation (e.g., Schutz 2009). However, for practical purposes, we recast the equations in a form more amenable for the Monte Carlo algorithm. The calculation proceeds as follows. For each spatial step of length $\Delta\ell$, the coordinate system is rotated to a frame where $\hat{x} = \hat{r}$ and $\hat{z} = \hat{r} \times \hat{k}$, e.g., the usual $\theta = \pi/2$ plane (see Appendix A for the explicit transformation). We then integrate, as a function of azimuthal angle, the geodesics for the radial coordinate r , the components of \hat{k} in a non-coordinate orthonormal polar basis, $\hat{k} = k^{\hat{r}}\hat{r} + k^{\hat{\phi}}\hat{\phi}$, where $\hat{r} = \sqrt{(1-r_s/r)}\vec{e}_r$ and $\hat{\phi} = \vec{e}_{\phi}/r$ (e.g., Schutz 2009), and the line segment traversed Δs . Here and throughout the paper, $r_s \equiv 2GM_{\text{NS}}/c^2$. The ordinary differential equation system is

$$\frac{dr}{d\phi} = r \sqrt{1 - \frac{r_s}{r}} \left(\frac{k^{\hat{r}}}{k^{\hat{\phi}}} \right) \quad (29)$$

$$\frac{dk^{\hat{r}}}{d\phi} = \frac{k^{\hat{\phi}}}{\sqrt{1 - r_s/r}} \left[1 - \frac{3}{2} \frac{r_s}{r} \right] \quad (30)$$

$$\frac{dk^{\hat{\phi}}}{d\phi} = -k^{\hat{r}} \sqrt{1 - \frac{r_s}{r}} \left[1 - \frac{1}{2} \frac{r_s/r}{(1 - r_s/r)} \right] \quad (31)$$

$$\frac{ds}{d\phi} = \sqrt{\left(\frac{dr}{d\phi} \right)^2 + r^2}. \quad (32)$$

We have tested our implementation by verifying agreement with the asymptotic expansion of Beloborodov (2002), which is accurate to about 1 part in 10^{-3} .

⁷ It would affect scattering for either very high energy photons, very energetic particle distributions, or ion scattering. In the case of polarization transfer, propagation close to the star is well inside the adiabatic limit; see §2.1.3.

Within the code, the problem is of boundary value type, as we require the line segment traversed Δs to equal the externally imposed step size $\Delta \ell$. This is needed so that a backwards and forward step sequence (e.g., for spatial derivatives of the magnetic field) returns to the original position. In practice, we have found that a simple 3-step iterative process achieves this equality to double precision in most cases. The initial angular interval for the Runge-Kutta integrator is estimated as $\Delta \phi_1 = \Delta \ell / \sqrt{r^2 + (dr/d\phi)^2}$. Subsequent corrections are then $\Delta \phi_{i+1} = (\Delta \ell - \Delta s_i) / \sqrt{r_i^2 + (dr/d\phi)_i^2}$, where i is the order of the iteration. Despite these simplifications, combined solution of equations (21)-(22) and (29)-(32) becomes computationally expensive when $\gtrsim 10^7$ photons are followed. We thus cut off light bending when $r_s/r < 2 \times 10^{-2}$, i.e., when general relativity modifies the trajectory to less than 1%, and impose planar propagation outside that radius.

3.2. Scattering

Aside from taking $\bar{\beta}$ out of the square brackets in equation (12), the scattering algorithm remains the same as in Fernández & Thompson (2007), including the adaptive step size algorithm in momentum space.

The overlap of the photon polarization with a circularly polarized wave $|e_{\pm}|^2$, which enters the optical depth (eq. [12]), needs to be modified for the possibility of non-adiabaticity,

$$\begin{aligned} |e_{\pm}|^2 &= \frac{1}{2} \left| \mathbf{A} \cdot \left(\mu_r \hat{x} - \sqrt{1 - \mu_r^2} \hat{z} \pm i \hat{y} \right) \right|^2 \\ &= \frac{1}{2} [\mu_r \text{Re}(A_x) \mp \text{Im}(A_y)]^2 \\ &\quad + \frac{1}{2} [\mu_r \text{Im}(A_x) \pm \text{Re}(A_y)]^2, \end{aligned} \quad (33)$$

where $\hat{k} = \hat{z}$, and the magnetic field lies in the x - z plane. Thus, when modes are coupled, the sign of the charge needs to be taken into account.

3.3. Polarization Evolution

Since $\ell_A \propto B^{-2}$, this length scale can become very small at radii $r \ll r_{\text{pl}}$, hence integration of equations (21)-(22) becomes impractical in regions where adiabatic propagation is a good approximation. An arbitrary choice has to be made for the transition surface where the ordinary differential equation solver is turned on. Once this choice is made, we set the initial conditions for the integration such that the absolute value of the components of the electric field correspond to those of the normal mode the photon was in before reaching the transition surface. A single random complex phase is then assigned to all components.

Figure 3 shows the real part of the electric field vector relative to the magnetic axis for a test E-mode photon moving outwards along the x -axis, in a magnetosphere with a twist $\Delta \phi_{\text{NS}} = 1$. Integration of equations (21)-(22) begins at

$$\eta_{\text{couple}} \equiv \frac{\ell_A}{r} = 10^{-3}, \quad (34)$$

corresponding to a radius $r \simeq 40R_{\text{NS}}$ on the equatorial plane. As the photon travels out, the characteristic spatial oscillation frequency of \mathbf{A} becomes longer, and the polarization reaches its asymptotic value at a distance $\sim 200R_{\text{NS}}$ from the star. In

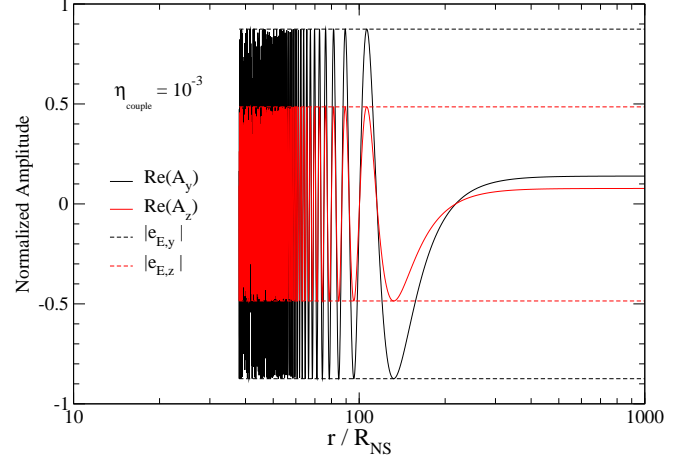


FIG. 3.— Real components of the electric field (solid lines) and normal mode eigenvectors (dashed-lines) for a test E-mode photon moving radially outward along the x -axis. Integration of equations (21)-(22) begins when $\eta_{\text{couple}} = 10^{-3}$ (eq. [34]). The photon stays in the same normal mode because the component of \mathbf{B} transverse to the propagation does not change direction.

this particular case, because the trajectory is radial, the component of the magnetic field perpendicular to the trajectory does not change direction, thus normal modes should not couple (c.f. eq. [24]). Figure 3 shows that the amplitude of the oscillations in \mathbf{A} are bracketed by the absolute value of the corresponding polarization eigenvector, hence our integration correctly captures adiabatic propagation. This purity of normal mode state is achieved to double precision for radial propagation, as measured by the intensity in the orthogonal mode.

Figure 4 shows the effect of changing the value of η_{couple} for a test E-mode photon moving along $\mathbf{r} = 18R_{\text{NS}}\hat{x} + \lambda(\hat{x} + \hat{y} + \hat{z})$, where $\lambda > 0$ is a parameter labeling the trajectory⁸. Because adiabatic propagation is captured with good accuracy, there is no significant difference in starting the integration as deep as $\eta_{\text{couple}} = 10^{-5}$, corresponding roughly to a factor two in distance relative to $\eta_{\text{couple}} = 10^{-3}$, showing that the final photon state is converged.

As the photon moves out, the polarization tensors (eqns. [18]-[19]) smoothly approach unity, with a consequent freezing of the electric field vector. Figure 4a shows that the absolute value of the spatial components of \mathbf{A} relative to the magnetic axis cease to vary significantly at radii $\sim 200R_{\text{NS}}$. Nonetheless, a quantitative criterion is needed to establish freezing in practice. As a figure of merit, we measure the norm of the difference between the polarization vector before and after each spatial step

$$|\Delta \mathbf{A}| = |\mathbf{A}(\mathbf{r} + \Delta \ell \hat{k}) - \mathbf{A}(\mathbf{r})|, \quad (35)$$

and then proceed to multiply this quantity by the factor $(r/\Delta \ell)$, obtaining an estimate of the change in \mathbf{A} over a scale height in magnetic field strength. The result is shown in Figure 4b. The dashed line shows the point where $|\Delta \mathbf{A}|(r/\Delta \ell) = 10^{-3}$, which we establish as our fiducial criterion for polarization freezing. As shown by Figure 5, this rather conservative limit is located at distances $< 1000R_{\text{NS}}$ from the star for most trajectories, safely below the light cylinder by at least an order of magnitude. It also lies below the point where the plasma

⁸ We ignore light-bending in Figures 4 and 5.

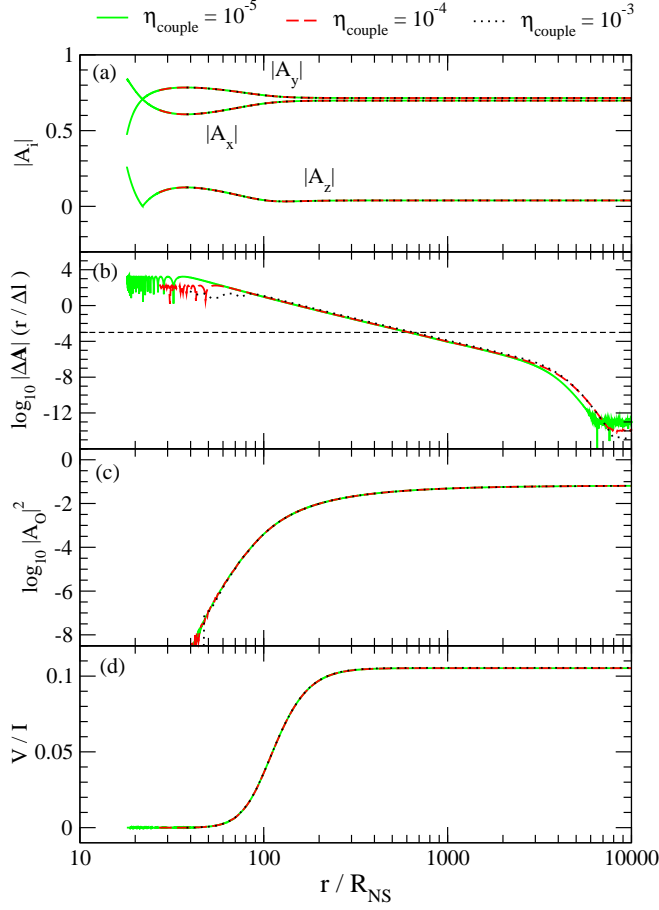


FIG. 4.— Various quantities for a test E-mode photon moving along the line $18R_{\text{NS}}\hat{x} + \lambda(\hat{x} + \hat{y} + \hat{z})$ relative to the magnetic axis, where $\lambda > 0$ is a parameter labeling the trajectory. Different curves correspond to different values η_{couple} above which the polarization evolution equations (21)–(22) are solved. Panels show, as a function of radial distance from the star, (a) the absolute value of the electric field vector components relative to the magnetic axis, (b) the approximate change of the polarization vector over one magnetic field scale-height, (c) the projection of the electric field onto the O-mode eigenvector, and (d) the normalized Stokes V parameter (eq. [39]). The dashed line shows the value of the electric field change at which we consider the polarization frozen (see text for details).

contribution would become comparable to that of the magnetized vacuum (eq. [17]).

Figure 4(c)–(d) also illustrates how normal modes become coupled in a non-radial trajectory. Panel (c) shows the normalized intensity in the O-mode, $|A_O|^2 = |\mathbf{A} \cdot \hat{e}_O|^2$ with \hat{e}_O the O-mode eigenvector, while panel (d) shows the normalized Stokes V component (eq. [39]). Modes begin to couple within a factor 2 of the polarization limiting radius (eq. [27]), before the electric field components freeze. This particular trajectory asymptotes to a $\sim 10\%$ amplitude in the orthogonal mode, and a circular polarization component of the same magnitude, showing the importance of solving equations (21)–(22).

As a further test of our implementation, we have calculated the polarization signal as a function of phase for two configurations with $\Delta\phi_{\text{NS}} = 0$ (no scattering), light bending, and other parameters mirroring Figures 7 and 8 of Heyl et al. (2003)⁹. The latter are equivalent to a configuration with stellar radius $R_{\text{NS}} = 10$ km, a polar magnetic field $B_{\text{pole}} = 2 \times 10^{12}$ G,

⁹ The panel in the lower left could only be matched to the corresponding Figure in Heyl et al. (2003) by changing the orientation angles.

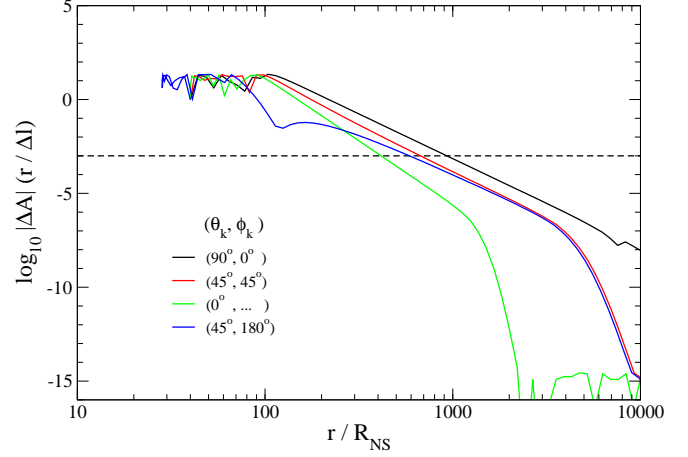


FIG. 5.— Norm of the change in the polarization vector over a scale height in magnetic field (eq. [35]) for various trajectories, labeled by the direction of the wave vector \hat{k} relative to the magnetic axis. The latter is parameterized in terms of the polar and azimuthal angles θ_k and ϕ_k , respectively. Photons start from $\mathbf{r} = 40R_{\text{NS}}\hat{x}$, and their wave vector points towards \hat{x} (black), $[\hat{x} + \hat{y} + \hat{z}]$ (red), \hat{z} (green), and $[-\hat{x} + \hat{z}]$ (blue). The latter trajectory crosses the z -axis. The horizontal dashed line marks the point where we consider the polarization to be effectively frozen.

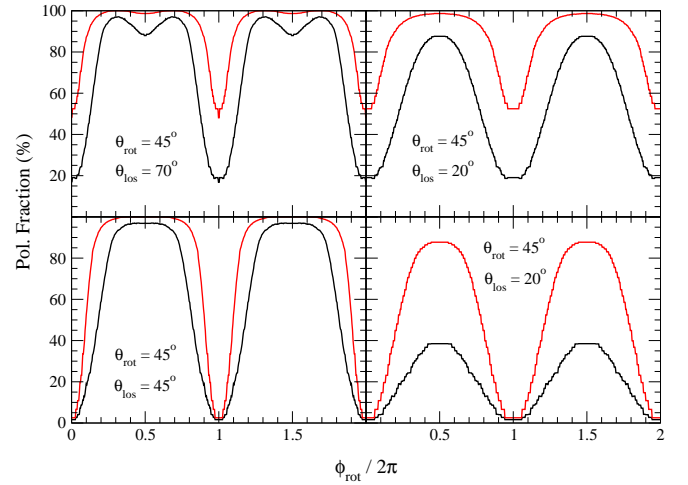


FIG. 6.— Polarization fraction for monoenergetic photons and dipolar field (no scattering) as a function of phase for different relative orientations of magnetic axis, rotation axis, and line-of-sight (eqns. [42] and [43]). Parameters are $R_{\text{NS}} = 10$ km, $B_{\text{pole}} = 2 \times 10^{12}$ G, and $\hbar\omega = 6.626$ eV (black) and 0.6626 keV (red). Results agree with Figures 7 and 8 of Heyl et al. (2003).

and monoenergetic photons with energy $\hbar\omega = 6.626$ eV and 0.6626 keV, respectively.

3.4. Postprocessing

Once the photon polarization is frozen, we store its frequency, position, direction, and polarization vectors. In contrast to Fernández & Thompson (2007), we do not convolve a frequency shift distribution with a blackbody function, but instead directly draw photons from a Planck distribution. The convolution of a frequency independent shift distribution with a source function is incompatible with the fact that the polarization evolution equations depend explicitly on the photon frequency through k_0 (eqns. [21]–[22]).

In addition to the aforementioned variables, we keep track of the number of scatterings a photon has had before escaping,

TABLE 1
MODEL PARAMETERS

| Name ^a | Dist. ^b | $\Delta\phi_{\text{NS}}$ (rad) | γ_{max} | Seed Pol. | θ_{cap} (°) | Fig. |
|-------------------|--------------------|--------------------------------|-----------------------|-----------|---------------------------|-------|
| t10 g20 c90 Eu | uni | 1 | 2 | E-mode | 90 | 7-20 |
| t10 g20 c90 Eb | bid | 1 | 2 | E-mode | 90 | 12 |
| t08 g24 c90 Eu | uni | 0.8 | 2.4 | E-mode | 90 | 13,18 |
| t12 g18 c90 Eu | uni | 1.2 | 1.8 | E-mode | 90 | 13,18 |
| t14 g17 c90 Eu | uni | 1.4 | 1.65 | E-mode | 90 | 13,18 |
| t16 g16 c90 Eu | uni | 1.6 | 1.6 | E-mode | 90 | 13,18 |
| t10 g20 c90 Ou | uni | 1 | 2 | O-mode | 90 | 15,19 |
| t10 g20 c5b Eu | uni | 1 | 2 | E-mode | 5 (both) | 16,20 |
| t10 g20 c5s Eu | uni | 1 | 2 | E-mode | 5 (south) | 16,20 |
| t10 g20 c5p Eu | uni | 1 | 2 | E-mode | 5 (planar) | 16,20 |

^aWe do not list here models with $\Delta\phi = 0$, or test calculations.

^bDirectionality of the particle energy distribution (eq. [7]), with *uni* denoting uni-directional, and *bid* bidirectional, respectively.

and construct separate histograms labeled by this parameter.

The standard parameterization of polarization degrees of freedom is a set of four Stokes parameters (e.g., Rybicki & Lightman 2004). Choosing the photon direction as the \hat{z} axis, there is an additional degree of freedom in their definition: the rotation angle around this axis. Choosing a coordinate system where the magnetic field is initially in the $x-z$ plane, we can write

$$I = |A_x|^2 + |A_y|^2 \quad (36)$$

$$Q = |A_x|^2 - |A_y|^2 \quad (37)$$

$$U = 2\text{Re}(A_x A_y^*) \quad (38)$$

$$V = 2\text{Im}(A_x A_y^*), \quad (39)$$

where the star stands for complex conjugation, and I measures the intensity, Q and U linear polarization, and V circular polarization. Standard observables are the linear polarization fraction¹⁰

$$\Pi_L = \frac{\sqrt{Q^2 + U^2}}{I}, \quad (40)$$

and the polarization angle

$$\chi = \frac{1}{2} \arctan\left(\frac{U}{Q}\right). \quad (41)$$

Rotation of the Stokes parameters around the z -axis is straightforward (e.g., Chandrasekhar 1960), and involves only Q and U . For phase dependent quantities, we perform a rotation such that the x -axis is in the plane of the line of sight and the rotation axis.

Quantities as a function of phase are obtained by performing suitable geometric transformations (Appendix A), which have as input parameters the two orientation angles

$$\cos\theta_{\text{rot}} = \hat{M} \cdot \hat{\Omega} \quad (42)$$

$$\cos\theta_{\text{los}} = \hat{O} \cdot \hat{\Omega}, \quad (43)$$

where \hat{M} , $\hat{\Omega}$, and \hat{O} are the magnetic axis, rotation axis, and line of sight direction, respectively¹¹.

¹⁰ We focus on linear over full polarization fraction because photoelectric polarimeters will not be sensitive to circular polarization (e.g., Swank et al. 2010).

¹¹ These two angles are denoted respectively by ξ and χ in Nobili et al. (2008).

3.5. Model Parameters

Table 1 shows the sequence of models investigated in this paper. All of them cover the energy range 0.04–40 keV. We run two versions of each. One with 40 bins per decade in energy and 64 bins in $\cos\theta_k$, optimized for angle-averaged studies as a function of energy. We also compute models with 10 bins per decade in energy and 256 bins in angle, to compute frequency integrated lightcurves. Because the magnetic field is axisymmetric, we average our results in ϕ_k . The number of seed photons is such that there are 10^4 per energy-angle bin. The stellar radius is assumed to be $R_{\text{NS}} = 10$ km, the Schwarzschild radius $R_{\text{NS}}/r_s = 3$, the magnetic field at the poles $B_{\text{pole}} = 10^{14}$ G, and the temperature of the seed blackbody measured at infinity $kT_{\infty} = (1 - r_s/R_{\text{NS}})^{1/2} kT = 0.4$ keV. Other parameter combinations for each model are listed in Table 1. Model names refer to their twist angle (t), maximum Lorentz factor (g), polar cap radius (c), seed polarization (E/O), and directionality (u/b).

4. RESULTS

Since one of our primary goals is to provide predictions for future X-ray polarimeters like GEMS, we focus on the behavior of the linear polarization fraction (eq. [40]) and polarization angle (eq. [41]) in relation to the total intensity, as different system parameters are changed. Phase-integrated and phase-dependent observables provide complementary information about the system, and we consider each class of measurement in turn. Due to rotation, both sets of observables depend on the relative orientation of rotation axis, magnetic axis, and line-of-sight, as parameterized by the angles θ_{rot} and θ_{los} (eqns. [42] and [43], respectively). Therefore, we begin by discussing the emission in the corotating frame, where the physics giving rise to the polarization signal is most easily understood.

4.1. Polarized Emission in the Corotating Frame

We first focus on the basics of the angular and frequency distribution of the polarized emission in the corotating frame. Figure 7 shows two-dimensional histograms of intensity, polarization fraction, and polarization angle measured at infinity, as a function of photon energy and magnetic colatitude, for model t10 g20 c90 Eu. For illustration, we have separated out in different columns the contributions from scattered and unscattered photons, plus their sum.

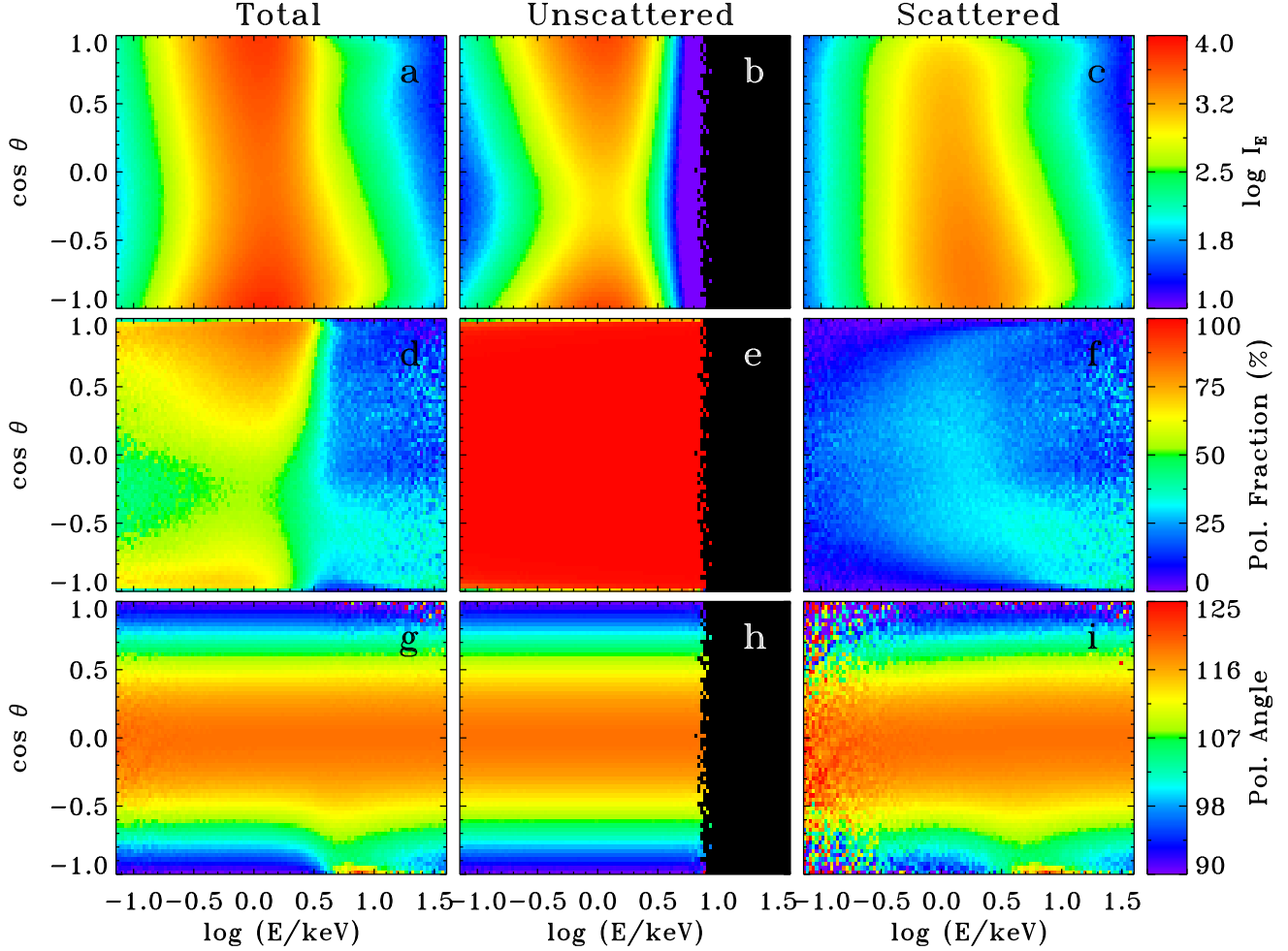


FIG. 7.— Observables measured at infinity for model t10 g20 c90 Eu, as a function of photon energy and magnetic colatitude. Each panel shows, from top to bottom, number of photons collected, linear polarization fraction (eq. [40]), and polarization angle (eq. [41]), respectively. Left, middle, and right panels correspond to the total, unscattered, and scattered contributions, respectively. Regions of parameter space with no counts are shown in black.

Panels (a)-(c) of Figure 7 show the number of photons collected at infinity. The unscattered distribution has an energy dependence close to that of a blackbody¹² and an angular dependence given by $I_{\text{unscatt}} = I_0 e^{-\tau(\theta)}$, where I_0 is the surface intensity and $\tau \sim \sin^2 \theta \Delta\phi / \bar{\beta}$ the total optical depth (the integral along the line-of-sight of eq. [12]). The exact dependence of the latter on magnetic colatitude and the unidirectional particle velocity distribution introduce a slight north-south asymmetry. The scattered component, on the other hand, peaks at the southern hemisphere. This results from the fact that photons with a large positive energy shift move out of the magnetosphere when they are generated close to the magnetic equator, where the magnetic field points downwards. Upscattered photons moving northward are re-entering the magnetosphere (see below). At fixed magnetic colatitude, the frequency dependence is smooth curve and extends to both sides of the original blackbody peak.

Panels (d)-(f) of Figure 7 show the corresponding polarization fractions. The unscattered component reflects the po-

larization distribution of seed photons, in this case 100% E-mode. The scattered component has a characteristic polarization fraction of $\sim 30\%$, which arises mostly from mode exchange (see below). The total polarization fraction peaks at the north pole, because more unscattered photons leave in that direction, and they are more polarized. This is the consequence of having a uni-directional particle energy distribution, which causes a break of the north-south symmetry. Thus, the polarization fraction carries a signature in both energy and angle.

From equation (16), one can see that photons are more likely to be in the E-mode state immediately after scattering, for all $|\mu_r| < 1$. This, coupled with nearly adiabatic propagation, means that E-mode polarization dominates the scattered emission for all values of the energy and magnetic colatitude. If photons were to scatter only once, the net polarization fraction would be

$$\Pi_L = \int \left[\frac{1 - (\mu'_r)^2}{1 + (\mu'_r)^2} \right] [1 + (\mu'_r)^2] d\mu'_r \bigg/ \int [1 + (\mu'_r)^2] d\mu'_r = 0.5, \quad (44)$$

where the weight $[1 + (\mu'_r)^2]$ comes from the total differential cross-section (eq. [13]). The characteristic polarization

¹² The optical depth (eq. [12]) depends implicitly on frequency through the resonant momenta $(\gamma\beta)^\pm$.

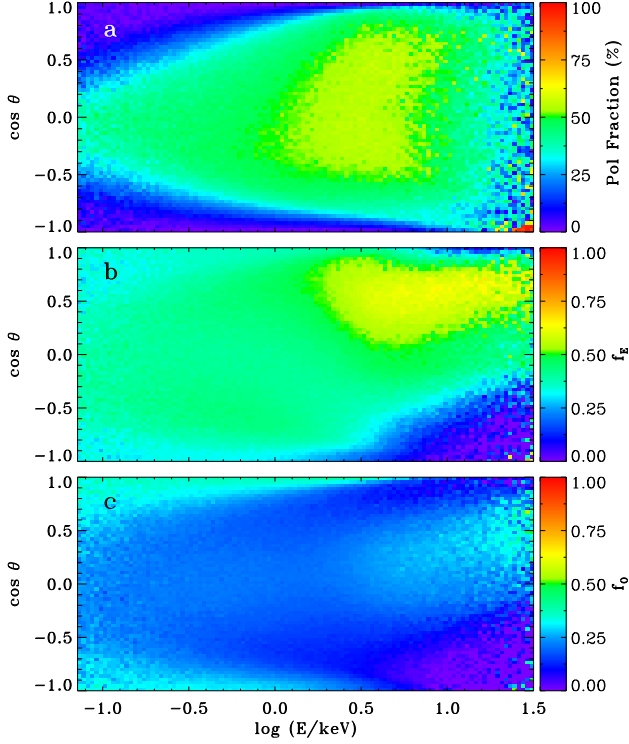


FIG. 8.— *Top*: Polarization fraction in the first scattering order for a run with the same parameters as model t10 g20 c90 Eu, but forcing photons to escape after one scattering. *Middle and Bottom*: Fraction of re-scattered E- and O-mode photons, respectively, obtained by subtracting the normal mode intensities of model t10 g20 c90 Eu (which undergoes multiple scattering) from the corresponding values from the run shown in the top panel (with a single scattering). As E-mode photons have a larger cross-section, they undergo relatively more re-scatterings than O-mode photons and hence the polarization fraction decreases from the upper limit given by equation (44).

fraction of $\sim 30\%$ observed at infinity arises from multiple scattering. In particular, E-mode photons have a larger cross-section than O-mode photons at all angles because of the overlap $|e_{\pm}|^2$ (eqns. [14] and [33]), and hence they are more likely to undergo further scatterings, decreasing the overall polarization fraction.

To show this effect, Figure 8(a) displays the polarization fraction of the scattered component in a run with the same parameters as model t10 g20 c90 Eu (Figure 7) but this time forcing photons to escape after their first scattering. The average polarization fraction is consistent with what equation (44) predicts. One can take the difference between the normal mode intensities in this run and those from the first scattering order in model t10 g20 c90 Eu to find the fraction of re-scattered photons. The resulting numbers for E- and O-mode are shown in panels (b) and (c) of Figure 8. As expected, E-mode photons undergo relatively more re-scatterings than O-mode photons, decreasing the overall polarization fraction of the first scattering order while still dominating the output. The bulk of re-scattering affects photons that move towards the north magnetic pole and have a high energy. The maximal frequency boost imparted by equation (8) is $(1 + \beta\mu_{\text{in}})/(1 - \beta\mu_{\text{out}})$, with $\mu_{\text{in}} > 0$ and $\mu_{\text{out}} > 0$ the ingoing and outgoing cosine between photon direction and magnetic field ($\beta > 0$ in the uni-directional case). Hence these photons correspond to those who first scattered closer to the south

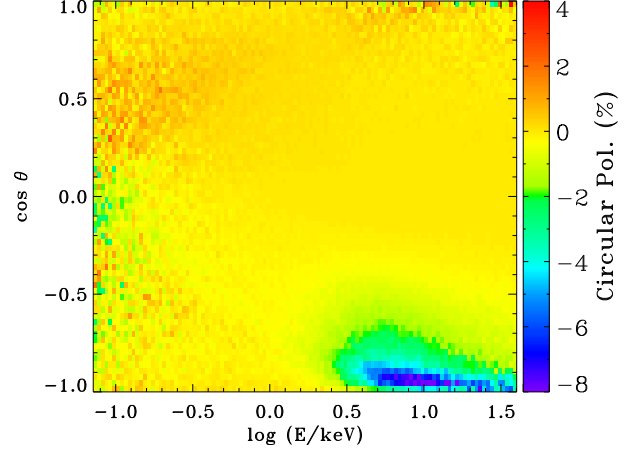


FIG. 9.— Circular polarization fraction measured at infinity (normalized Stokes V parameter, eq. [39]) for model t10 g20 c90 Eu, as a function of photon energy and magnetic colatitude.

magnetic axis, where the magnetic field points mostly northward, and whose value of μ changed from negative to positive. After their first scattering, these photons move inwards, being most likely to scatter again. An analogous argument shows why high-energy photons going southward after scattering are the most likely to escape.

Panels (g)-(i) of Figure 7 show the polarization angle. It is immediately evident that this quantity is mostly independent of energy for this particular case, varying only with magnetic colatitude, aside from a small region of scattered emission near the south pole. Absent twist, the magnetic field is dipolar and parallel to the magnetic axis along the line-of-sight. This would yield a polarization angle of 90° for the E-mode and 0° for O-mode. A positive $\Delta\phi_{\text{NS}}$ introduces a dependence on magnetic colatitude, increasing these values away from the poles. The functional form is equal, within statistical errors, to the angle that the magnetic field makes with the magnetic axis. For model t10 g20 c90 Eu and measured relative to the magnetic axis, the polarization angle is $\chi = \arctan(B_\phi/B_\theta) + \pi/2$.

The weak dependence on energy results from E-mode polarization dominating the scattered component at most angles and energies, combined with the assumption of E-mode seed photons in the t10 g20 c90 Eu model. This dominance of the E-mode in the scattered emission persists even if 100% O-mode seed photons are used. The only difference is a 90° jump as a function of energy when transitioning to the unscattered component. The polarization vector follows the local magnetic field direction adiabatically until the coupling region at $r \sim r_{\text{pl}} \sim 100R_{\text{NS}}$ (eq. [27]).

Figure 9 shows the degree of circular polarization for model t10 g20 c90 Eu as a function of energy and magnetic colatitude. It is produced almost exclusively by the scattered component, and its value deviates from zero by a few percent throughout the energy-colatitude plane, except in regions close to the magnetic poles at high energies. The maximum absolute value of about 8% is reached near the south pole, towards which most scattered photons with a positive energy shift escape.

In principle, any photon moving non-radially will develop

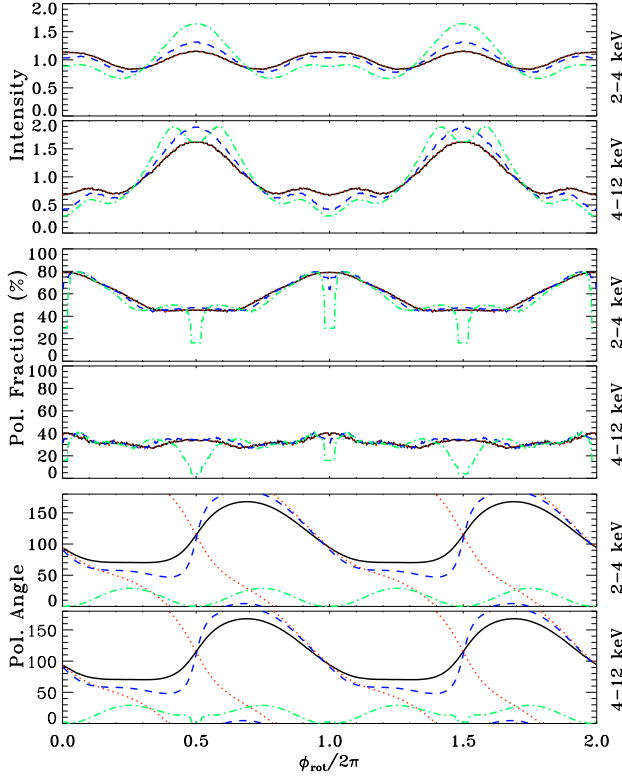


FIG. 10.— Intensity (top), polarization fraction (middle), and polarization angle (bottom) as a function of rotational phase ϕ_{rot} in two energy bands (2-4 keV and 4-12 keV) for model t10 g20 c90 Eu and various viewing geometries. The curves correspond to pairs of angles $(\theta_{\text{rot}}, \theta_{\text{los}})$ of $(45^\circ, 70^\circ)$: solid/black), $(70^\circ, 45^\circ)$: dotted/red), $(60^\circ, 70^\circ)$: dashed/blue), and $(90^\circ, 90^\circ)$: dot-dashed/green). For illustration, two full periods are shown.

a circular polarization component as it traverses the magnetosphere (e.g., Figure 4[c]). To see this, one can write an equation for the rate of change of V along the photon trajectory, by combining equations (21), (22), and (39). After some algebra, one finds that to leading order in $\delta = \alpha_{\text{em}}(B/B_{\text{QED}})^2/(45\pi)$ one has

$$\frac{\partial V}{\partial z} = (q+m) \sin^2 \theta_{kB} \cos 2\phi_{kB} U + O(\delta^2), \quad (45)$$

where θ_{kB} and ϕ_{kB} are respectively the polar and azimuthal angle of the magnetic field in a coordinate system where $\hat{k} = \hat{z}$ and \hat{B} is in the x-z plane. If the polarization vector is in a normal mode state, then $U = 0$ and no circular component is generated. Similarly, $dV/dz = 0$ if photons propagate parallel to the magnetic field.

The fact that the unscattered component has V almost identically zero everywhere is due to the fact that a given non-radial trajectory originating from the star always has a counterpart for which the magnetic field rotates in the other direction along the trajectory, cancelling out the net contribution to V if they have the same intensity. The scattered component, however, is not isotropic and thus such cancellation does not occur, leaving a residual circular polarization signal. If plasma polarization were to become dominant at some radius comparable to r_{pl} (eq. [27]), then the circular polarization fraction could be much higher and substantially modify the outgoing linear polarization signal.

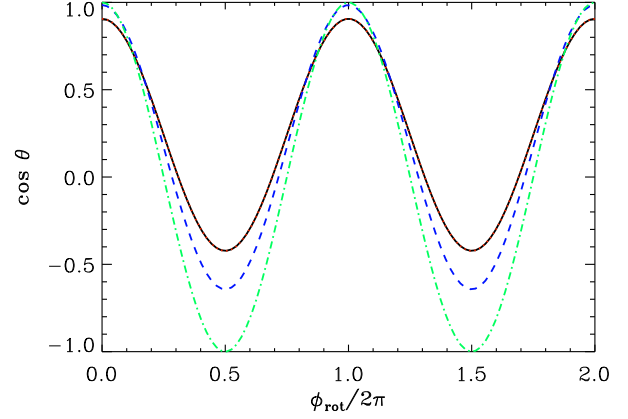


FIG. 11.— Magnetic colatitude swept by the line-of-sight as a function of rotational phase for various viewing geometries. The color and line styles have the same meanings as in Figure 10.

4.2. Phase-resolved Emission

Ideally, one would like to observe the system from all angles in the corotating frame and generate observed maps as a function of magnetic colatitude for comparison with plots like Figure 7. In practice, we have a fixed line of sight for any single source, so that the viewing angle corresponds to a time varying magnetic colatitude as a function of rotational phase ϕ_{rot} . Due to this relatively direct relationship with the corotating frame observables, we find it pedagogically advantageous to discuss phase-resolved observables first. This relationship also means that polarization measurements as a function of rotational phase yield the most detailed information about the system. Hence, they are the most useful observational constraints for disentangling geometrical effects from the physics of the surface and magnetosphere. However, they may necessitate much longer integration times to achieve useful signal-to-noise. We discuss prospects for obtaining such phase-resolved measurements with GEMS in §5.

Figure 10 shows several light curves corresponding to the t10 g20 c90 Eu model for different lines-of-sight and magnetic axis orientations. The phase is defined so that the north and south magnetic poles cross the line-of-sight at $\phi_{\text{rot}} = 0$ and π , respectively. Two full periods are shown for illustration. The intensity, polarization fraction, and polarization angle are computed after integrating the emission over a soft energy band (2-4 keV) that is dominated by direct emission, and a hard band (4-12 keV) which is mostly scattered flux. The normalization is chosen so that the average over phase is unity.

The variation of the total intensity and polarization fraction follows directly from the two dimensional map in Figure 7, as there is a simple mapping between rotational phase and magnetic colatitude (eq. [A7]). Figure 11 shows this mapping for the same set of orientations $(\theta_{\text{rot}}, \theta_{\text{los}})$ that are plotted in Figure 10. Orientation effects depend mostly on the maximum (most negative $\cos \theta$) observable colatitude, because the polarization fraction tends to be a minimum and the total intensity a maximum near the south magnetic pole. The mapping is invariant under the exchange $\theta_{\text{rot}} \leftrightarrow \theta_{\text{los}}$, so the solid black $(\theta_{\text{rot}} = 45^\circ, \theta_{\text{los}} = 70^\circ)$ and dotted red curves $(\theta_{\text{rot}} = 70^\circ, \theta_{\text{los}} = 45^\circ)$ are identical.

The orthogonal rotator viewed at $\theta_{\text{los}} = 90^\circ$ gives the largest

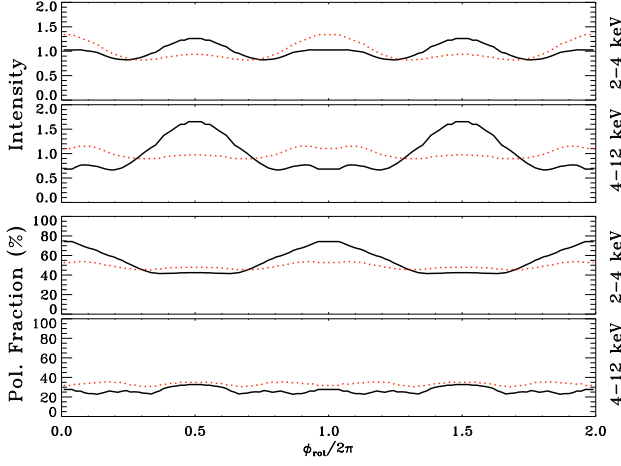


FIG. 12.— Intensity (top) and polarization fraction (bottom) as a function of phase in two energy bands (2-4 keV and 4-12 keV). The curves correspond to models t10 g20 c90 Eu (black solid) and t10 g20 c90 Eb (red dotted). The former assumes that the particle distribution is unidirectional, while that of the latter is bidirectional. Magnetic and viewing orientations corresponding to $\theta_{\text{rot}} = 45^\circ$ and $\theta_{\text{los}} = 70^\circ$ are assumed.

modulation. In this case the observer sees one of the magnetic poles directly at ϕ_{rot} equal to integer multiples of π . The optical depth to scattering is lowest along the poles, leading to dips in the total intensity at these phases. The polarization fraction is also low since the photon wave vector lies parallel to the magnetic field and there is no preferred direction for the polarization.

The gross, qualitative features of the total intensity and polarization fraction phase curves are largely insensitive to the orientation. There is a strong peak near $\phi_{\text{rot}} = \pi$ and generally a weaker one near $\phi_{\text{rot}} = 0$, when the south and north magnetic poles (respectively) cross the line-of-sight. The contrast is particularly clear in the hard energy band which is dominated by the scattered emission. However, in the soft band, which is dominated by the unscattered component the polarization fraction peaks near $\phi_{\text{rot}} = 0$ and has a minimum near $\phi_{\text{rot}} = \pi$.

The half period phase shift between the polarization fraction and the total intensity results from the assumption of a unidirectional photon distribution. Figure 12 shows a comparison of the t10 g20 c90 Eu and t10 g20 c90 Eb models. These differ only in their treatment of the particle distribution, with the latter having a bidirectional charge distribution. The largest contrast arises when comparing the intensity in the hard band with the polarization fraction in the soft band. The intensity and polarization fraction of the bidirectional model is completely symmetric in magnetic colatitude, so the differences between $\phi_{\text{rot}} = 0$ and π are purely orientation effects in this case¹³. In contrast to the unidirectional model, the peaks in intensity and polarization fraction coincide. Thus, one can distinguish whether the magnetosphere is filled with electron-positron or electron-ion pairs because this difference in particle distribution manifests itself as a break in the north-south symmetry for the unidirectional model.

As mentioned in §4.1, the polarization angle is determined primarily by the projection of the magnetic field at $r \sim r_{\text{pl}}$ onto the line-of-sight. In phase resolved plots, we have chosen the zero point for this angle to be the rotation axis, so

¹³ The observable colatitude range is $[25^\circ, 115^\circ]$

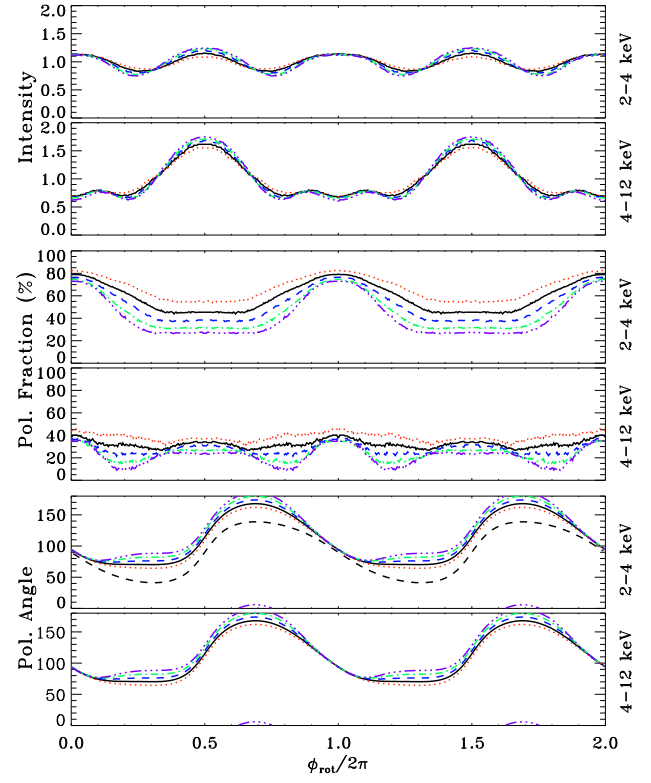


FIG. 13.— Intensity (top), polarization fraction (middle), and polarization angle (bottom) as a function of phase in two energy bands (2-4 keV and 4-12 keV) for different twist angles. The curves correspond to models t10 g20 c90 Eu (solid, black), t08 g20 c90 Eu (dotted, red), t12 g20 c90 Eu (blue, dashed), t14 g20 c90 Eu (green, dot-dashed), and t16 g20 c90 Eu (violet, triple-dot-dashed). Magnetic and viewing orientations corresponding to $\theta_{\text{rot}} = 45^\circ$ and $\theta_{\text{los}} = 70^\circ$ are assumed. For comparison, the long-dashed black line shows the polarization angle as a function of phase for a run with no twist and thus a purely dipolar field.

the absolute value will differ from that shown in Figure 7 by a geometric transformation involving θ_{rot} , θ_{los} , and the rotational phase ϕ_{rot} (eqns. [A7]-[A10]). This means that the phase curve of polarization angle is not affected by the invariance to $\theta_{\text{rot}} \leftrightarrow \theta_{\text{los}}$ exchange of the phase-colatitude mapping, as there is an additional rotation of the polarization vector as the magnetic axis rotates around the line-of-sight. This is seen most clearly by comparing the $(\theta_{\text{rot}} = 45^\circ, \theta_{\text{los}} = 70^\circ)$ and $(\theta_{\text{rot}} = 70^\circ, \theta_{\text{los}} = 45^\circ)$ curves in Figure 10. Although the intensity and polarization fraction phase curves are identical, the variation with polarization angle differs greatly between the two orientations. In general, for $\theta_{\text{rot}} < \theta_{\text{los}}$, the polarization oscillates about a mean value, while for $\theta_{\text{rot}} > \theta_{\text{los}}$ it sweeps through the full allowed range of 180° . This has important implications for the phase-averaged polarization, which we discuss below.

Figure 13 shows the variation of the phase-resolved observables as twist angle $\Delta\phi_{\text{NS}}$ and maximum Lorentz factor γ_{max} of the momentum distribution (eq. [7]) are varied. We are primarily interested in the variation with $\Delta\phi_{\text{NS}}$, but we vary γ_{max} simultaneously (see Table 1) to keep the power law slope of the spectrum as uniform as possible. As twist angle increases, the intensity increases for all energies above ~ 2 keV (c.f. §4.3) as the fraction of scattered photons increases. Thus the peak in the intensity near $\phi_{\text{rot}} = \pi$ becomes stronger in both bands.

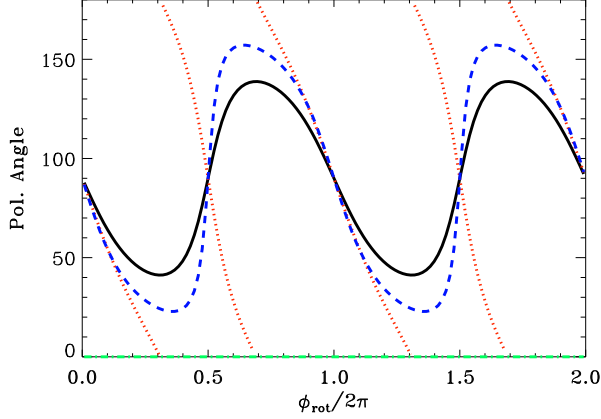


FIG. 14.— Polarization angle as a function of phase for a model with no twist (no scattering) and 100% E-mode seed photons for the same orientations as in Figure 10. Results for the soft and hard bands are identical due to lack of scattering, hence only one panel is shown. Note that the curves are symmetric every $1/2$ phase due to the dipolar geometry of the zero-twist field. A net twist angle of the field lines introduces an asymmetry for most orientations.

The polarization fraction shows the opposite trend with twist angle, however. As $\Delta\phi_{\text{NS}}$ increases, the polarization fraction gets smaller at every phase in both the soft and hard bands. For the soft band, the primary explanation is that scattered photons have lower polarization than unscattered, so that a larger fraction of scattered photons yields a lower overall polarization fraction. As with the intensity variation, the effect is again largest at $\phi_{\text{rot}} = \pi$, when the south pole crosses the line-of-sight. This result is qualitatively similar to that found by Nobili et al. (2008) using adiabatic propagation and taking the relative difference between the normal mode intensities to obtain polarization fractions. Nobili et al. (2008) averaged over magnetic colatitude and energy to obtain their result, and offered a similar interpretation.

However, it is notable that the drop in polarization fraction occurs even in the hard band. Unlike the soft band, it contains very little highly-polarized, unscattered emission, so the above explanation does not apply. Instead, the drop in polarization with increasing twist angle is due to the increased number of scatterings per photon, which remove relatively more E-mode than O-mode photons from the escaping beam along a given direction (see also §4.1).

For the orientation of Figure 13, the polarization angle oscillates about a mean value near 130° , with an overall shape that depends weakly on twist angle but which becomes more asymmetric as this parameter is increased. For reference, the black dashed curves in the panel corresponding to the soft band shows the variation in the polarization angle with phase for a model with $\Delta\phi_{\text{NS}} = 0$. In this case the oscillation is symmetric about 90° because the field is dipolar. Hence, asymmetry in the polarization angle is a direct indication of the presence of a twist angle at $r \sim r_{\text{pl}}$, and the magnitude of the asymmetry constrains the value of $\Delta\phi_{\text{NS}}$.

To illustrate this effect in more detail, Figure 14 shows the polarization angle that is obtained when the twist angle is set to zero, for the same set of orientations shown in Figure 10 (only one panel is shown, as the lack of scattering makes the results identical in both bands). Except for the orthogonal rotator, all curves in Figure 10 break the symmetry at $1/2$ phase relative to Figure 14, showing how the presence of a

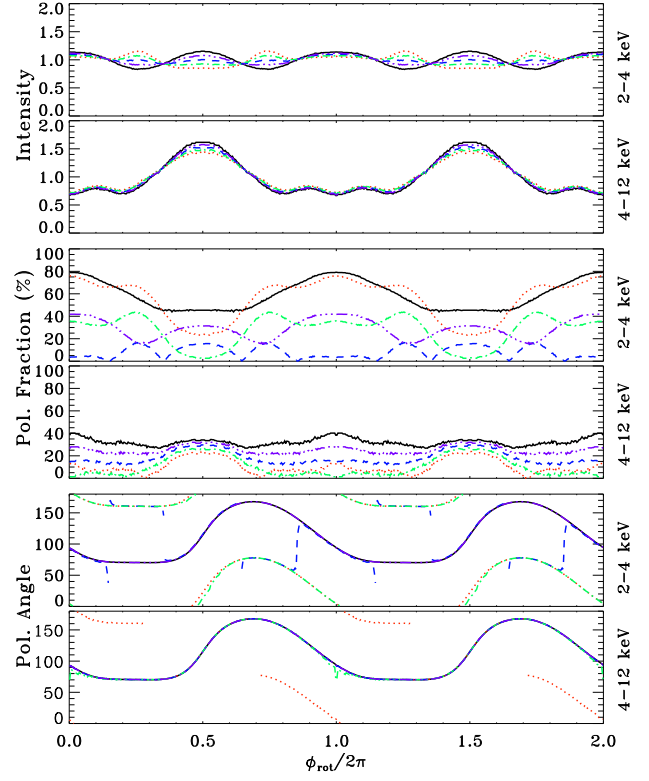


FIG. 15.— Intensity (top), polarization fraction (middle), and polarization angle (bottom) as a function of phase in two energy bands (2-4 keV and 4-12 keV) as the seed photon polarization is varied. The curves correspond to models with seed distributions that are 100% E-mode (solid, black); 100% O-mode (dashed, red); 50% E-mode + 50% O-mode (blue, dashed); 25% E-mode + 75% O-mode (green, dot-dashed); and 75% E-mode + 25% O-mode (purple, triple-dot-dashed). Magnetic and viewing orientations corresponding to $\theta_{\text{rot}} = 45^\circ$ and $\theta_{\text{los}} = 70^\circ$ are assumed.

net twist angle in the magnetosphere becomes directly measurable through the polarization angle. We emphasize that this effect is a more general consequence of the properties of QED eigenmodes (Heyl & Shaviv 2000), and only indirectly due to magnetospheric scattering in that a definite polarization mode becomes dominant. It would be worth exploring under what circumstances it is possible to uniquely reconstruct the magnetic field geometry from a given polarization angle curve; this work however lies beyond the scope of this paper.

We now consider the dependence of observables on the seed photon polarization, which so far has been 100% E-mode. Figure 15 shows the variation of the phase-resolved quantities as the polarization of the seed photon distribution varies. Only two models with 100% E-mode and O-mode seed polarization are directly computed (t10 g20 c90 Eu and t10 g20 c90 Ou, respectively). The linearity of the Stokes parameters allows us to combine these runs to get any partial polarization. Here we consider an unpolarized (50% E-mode, 50% O-mode) seed distribution and a two partially polarized (75% E-mode and 25% O-mode, 25% E-mode and 75% O-mode) to illustrate the trends. The soft band intensity changes because the optical depth has a different colatitude variation in the pure O-mode model (t10 g20 c90 Ou), due to the angular dependence in the overlap function $|e_{\pm}|^2$ (eqns. [14] and [33]). The hard band has a slightly weaker peak for the pure O-mode model due to the reduced scattering fraction. The unpolarized and partially polarized models lie between the pure polarization

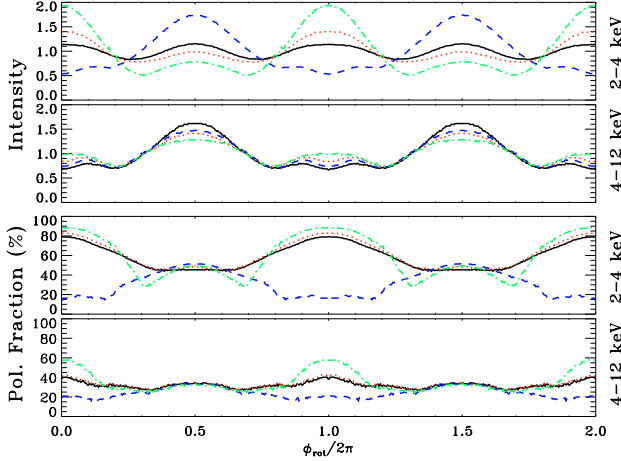


FIG. 16.— Intensity (top) and polarization fraction (bottom) as a function of phase in two energy bands (2-4 keV and 4-12 keV) for various assumptions about NS surface emission and photon propagation. The curves correspond to full surface emission with light bending included (t10 g20 c90 Eu, solid black), 5° polar cap on both magnetic poles with light bending (t10 g20 c5b Eu, dotted red), 5° polar cap with light bending but from the south pole only (t10 g20 c5s Eu, dashed blue), and 5° polar caps from both poles and planar propagation (t10 g20 c5p Eu, dot-dashed green). Magnetic and viewing orientations corresponding to $\theta_{\text{rot}} = 45^\circ$ and $\theta_{\text{los}} = 70^\circ$ are assumed.

models by construction.

The polarization fraction shows a somewhat stronger dependence on the seed photon distribution. For the pure O-mode model, the soft band polarization fraction is much weaker than the pure E-mode case at $\phi_{\text{rot}} = \pi$. This is because the transition from dominance of unscattered O-mode seeds to E-mode dominated scattered emission occurs within this band. As expected, the unpolarized and partially polarized models yield lower polarization fractions in the soft band, where unscattered photons dominate. The unpolarized model has a non-zero polarization fraction solely because of the non-negligible scattered emission towards lower energies. In the hard band, the scattered emission is E-mode dominated for all models, and the polarization fraction generally increases as the E-mode fraction of the seed photon increases.

In the soft band, which is dominated by unscattered photons, the phase curves of polarization angle for the models with pure E-mode and pure O-mode seeds differ by exactly 90° . The partially polarized models follow the curve of the dominant polarization, while the unpolarized model switches between the two. In the hard band, the pure E-mode and pure O-mode models yield identical polarization angles at some phases and differ by 90° at others. These discontinuous jumps occur in the 100% O-mode seeds case due to a colatitude-dependent transition from O-mode seeds to E-mode dominated scattered photons. The partially polarized and unpolarized models follow the E-mode curve.

Thus far all the models have assumed uniform emission of seed photons from the NS surface. Figure 16 illustrates the effects of confining emission to polar caps of 5° radius around the magnetic poles. In this case we only show the intensity and polarization fraction, as the polarization angle curves are identical. The solid (black) curves correspond to emission from the full surface (t10 g20 c90 Eu) while the red-dotted curves refer to a model with polar caps around both magnetic poles (t10 g20 c5bu). For the latter, there are modest enhancements and reductions of the intensity at $\phi_{\text{rot}} = 0$

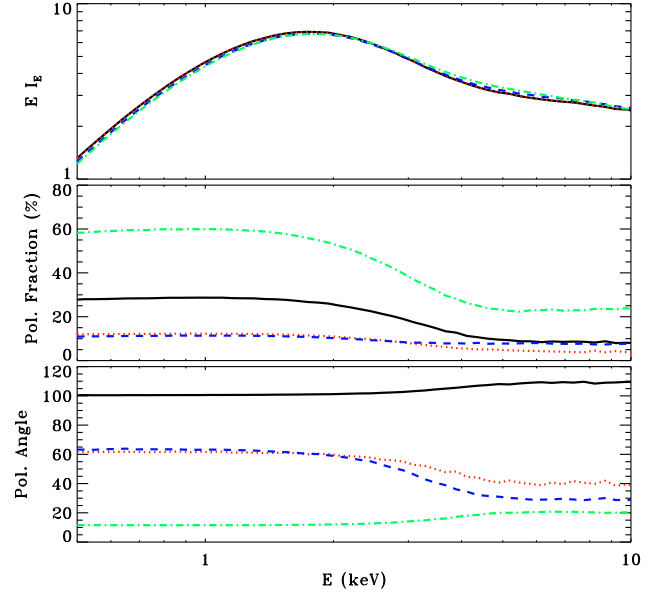


FIG. 17.— Phase-averaged intensity (top), polarization fraction (middle), and polarization angle (bottom) as a function of photon energy for model t10 g20 c90 Eu and various viewing geometries. The curves correspond to the same orientation angles as in Figure 10.

and π , respectively. This results primarily from the magnetic colatitude dependence of the scattering cross section, which is lowest near the poles.

Although there are these modest differences, the phase curves are remarkably similar for the two models, given the large differences in the fraction of the star that emits. Even though the polar cap emission is confined to a very small solid angle, light bending causes the NS to appear as a more isotropic emitter for observers several stellar radii from the star where much of the scattering occurs. For comparison, the green (dot-dashed) curves show a model with planar propagation and no light bending (t10 g20 c5pu). The differences with the isotropic emitter are much larger and there is much clearer signature in the polarization fraction.

Finally, we consider a case in which only the south magnetic pole radiates, including light-bending (t10 g20 c5su). This corresponds to the blue (dashed) curve in Figure 16. Since we have chosen an orientation in which the observer primarily sees the northern hemisphere, the lightcurve peaks at $\phi_{\text{rot}} = \pi$, when the south pole crosses the line-of-sight. When the north pole crosses our line-of-sight at $\phi_{\text{rot}} = 0$, there are very few unscattered seed photons, resulting in a low polarization fraction.

4.3. Phase-averaged Emission

Averaging quantities over stellar rotation yields higher signal-to-noise. Hence, phase-averaged measurements are likely to be the first (or perhaps only) constraints obtained when polarimeters become operational.

Figure 17 shows the t10 g20 c90 Eu model for the same orientation angles as in Figure 10. Independent of geometric arrangement, spectra show a decrease in the polarization fraction with energy as they transition from unscattered to scattering-dominated. This transition occurs over the range 2–4 keV, and involves a decrease in the net polarization fraction.

Although this decrease is generic, the precise value of the

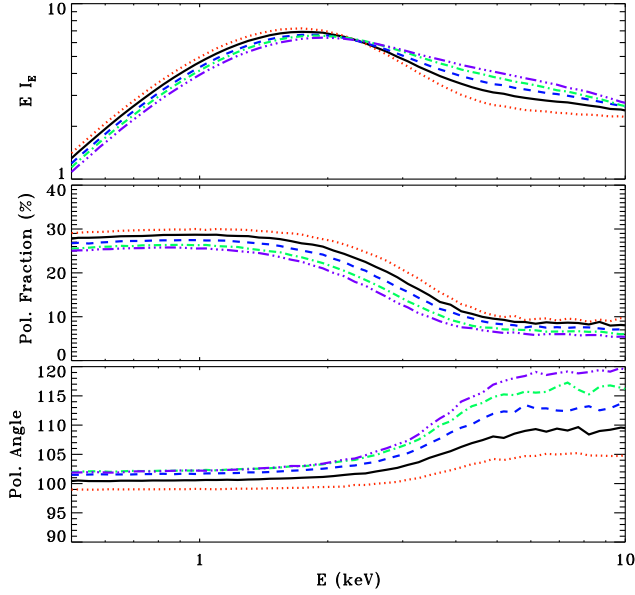


FIG. 18.— Phase-averaged intensity (top), polarization fraction (middle), and polarization angle (bottom) as a function of photon energy for models with different $\Delta\phi_{\text{NS}}$. Magnetic and viewing orientations corresponding to $\theta_{\text{rot}} = 45^\circ$ and $\theta_{\text{los}} = 70^\circ$ are assumed. Curves have the same meaning as in Figure 13.

polarization fraction and angle are orientation dependent. A comparison of the middle panels of Figures 10 and 17 shows that the phase-averaged polarization fraction is significantly more dependent on orientation than the corresponding phase curves. This is largely due to the phase dependence of the polarization angle, and is most clearly illustrated by the solid black ($\theta_{\text{rot}} = 45^\circ$, $\theta_{\text{los}} = 70^\circ$) and dotted red curves ($\theta_{\text{rot}} = 70^\circ$, $\theta_{\text{los}} = 45^\circ$) in the bottom panels of Figure 10. In general, for $\theta_{\text{los}} < \theta_{\text{rot}}$, the polarization angle tends to sweep out the full 180° range as the magnetic axis rotates on the plane of the sky. A larger polarization angle variation over a rotational period typically leads to a weaker phase averaged polarization fraction because the Stokes Q and U parameters have different signs at different rotational phases and tend to cancel. Indeed, the orthogonal rotator has the highest polarization fraction because the polarization angle shows the weakest phase dependence.

The variation of the phase-averaged polarization angle with energy is also orientation dependent. In practice, it is difficult to extract useful constraints from this quantity alone, since it is the phase dependence of the polarization vector, both angle and magnitude, that determines the phase-average. Rather different orientations can provide very similar rotation of the polarization angle with energy, while rather similar geometries can give significantly different results.

Figure 18 shows the variation of the phase-averaged observables with twist angle for the same orientation as in Figure 13. Note that there is some diversity in the shape of the spectra for the total intensity, even though we vary γ_{max} simultaneously with $\Delta\phi_{\text{NS}}$ to keep the high energy spectral slope approximately constant. As in the phase-resolved case, the polarization fraction decreases with increasing $\Delta\phi_{\text{NS}}$, but Figure 18 demonstrates that a drop in polarization fraction occurs for all photon energies. For increasing energy, the polarization angle rotates by an amount which increases monotonically with $\Delta\phi_{\text{NS}}$. In principle, this dependence could be used to probe

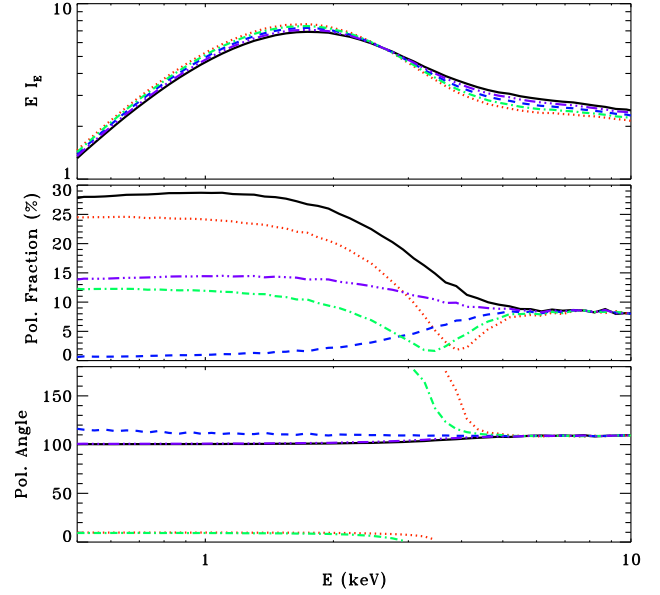


FIG. 19.— Phase-averaged intensity (top), polarization fraction (middle), and polarization angle (bottom) as a function of photon energy for models with different seed photon polarization. Magnetic and viewing orientations corresponding to $\theta_{\text{rot}} = 45^\circ$ and $\theta_{\text{los}} = 70^\circ$ are assumed. Curves have the same meaning as in Figure 15.

the twist angle, but the rotation of the polarization angle depends on the orientation as well, so this needs to be independently constrained.

Figure 19 compares the phase-averaged observables for different seed photon distributions, assuming the same orientation as in Figure 15. The curves correspond again to linear combinations of models t10 g20 c90 Eu and t10 g20 c90 Ou. At low energies ($\lesssim 2$ keV), the unpolarized and partially polarized seed photon distributions have low polarization fractions, as expected. The pure O-mode distribution has a lower linear polarization than the pure E-mode, because the small number of scattered photons at low energy with a net E-mode polarization which cancels some of the O-mode seeds. At higher energies (above ~ 5 keV), which are scattering dominated, mode exchange leads to a common value for the polarization fraction, independent of the seed distribution.

The variation of the polarization in the transition region from 2-5 keV is very sensitive to the seed photon distribution. As the t10 g20 c90 Ou model transitions from being dominated by O-mode seed photons to E-mode scattered photons, there is a clear drop and subsequent rise in the polarization, which coincides with a 90° rotation of the polarization. A similar trend is seen in the partially polarized, but O-mode dominated (75% O-mode, 25% E-mode) model. In contrast, the E-mode dominated models show a continuous decline, with only modest rotation of the polarization angle. Hence, observations of the polarization fraction as a function of photon energy in this transition region can discriminate clearly between predominately O-mode and predominately E-mode seed photons distributions. This would help elucidate the mechanism providing the dominant contribution to the thermal luminosity.

Figure 20 shows the effects of confining emission to polar caps. At high energies, the models all approach a common value for the polarization fraction. The differences in the fraction of scattered photons primarily drive the observed

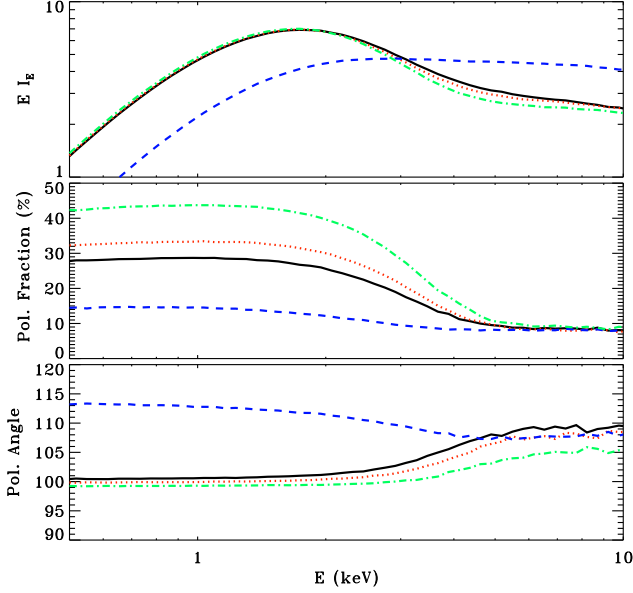


FIG. 20.— Phase-averaged intensity (top), polarization fraction (middle), and polarization angle (bottom) as a function of photon energy for various assumptions about NS surface emission regions and photon propagation. Magnetic and viewing orientations corresponding to $\theta_{\text{rot}} = 45^\circ$ and $\theta_{\text{los}} = 70^\circ$ are assumed. Curves have the same meaning as in Figure 16.

differences in the polarization fraction at low energies. The highly polarized seed photons tend to escape more easily along the poles, particularly when the effects of light bending are neglected. The exception is the model with emission from only the south pole, because the observer primarily sees scattered photons for the assumed orientation ($\theta_{\text{rot}} = 70^\circ$, $\theta_{\text{los}} = 45^\circ$). This also explains the large difference in the total intensity spectrum. An observer in the southern hemisphere (e.g. $\theta_{\text{los}} = -45^\circ$) would see spectra that are qualitatively similar to the other polar cap models. In contrast to the phase curves of the polarization angle, which were identical for the different models, the phase-averaged polarization angles differ due to the variation in the strength of polarization with rotational phase.

5. IMPLICATIONS FOR GEMS

We now perform simple estimates on the integration times required to obtain polarization information from magnetar candidates, based on current GEMS sensitivity parameters. The product of the GEMS effective area and modulation factor rises from zero at an energy of 2 keV to its maximum around 3 keV, and then decreases steadily, in such a way that by 6 keV it is smaller by a factor of three from the peak [T. Kallman, private communication; see also Swank et al. (2010)]. This and the typical form of magnetar candidate spectra implies that the bulk of the measured polarization signal will come from the transition between thermal and non-thermal parts of the spectrum. In §4 we showed that the polarization fraction in this region can have large variations depending on the polarization level of the surface emission (and the temperature of the blackbody, which we do not change in this study). According to our results, the non-thermal tail is expected to produce a more uniform and predictable polarization level, albeit at a significantly small flux level. Thus we base our estimates on trying to obtain a statistically significant measurement in this part of the spectrum, as it is the limiting

factor.

Following Weisskopf et al. (2010), we estimate uncertainties by assuming that the polarization noise follows a Poisson distribution. The 1-sigma uncertainty in the modulation amplitude measured by the detector when rotated around the line-of-sight is given by

$$\Delta a_{1\sigma} = 2 \sqrt{\frac{1}{N} \ln \left(\frac{1}{1-C} \right)} \bigg|_{C=0.68} = 2.1 \times 10^{-2} N_4^{-1/2}, \quad (46)$$

where N is the number of counts, $N_4 = N/10^4$, and C is the confidence level. The modulation amplitude produced by the source is

$$a_0 = m \Pi_L, \quad (47)$$

where m is the modulation of the detector, and Π_L is the linear polarization fraction (eq. [40]). We assume here that the contribution from the background is not important. Combining equations (46) and (47) allows determination of the number of counts needed to measure a_0 to within a given number of sigmas n_σ ,

$$N_\Pi = 4 \times 10^3 \left(\frac{n_\sigma}{3} \right)^2 \left(\frac{0.5}{m} \right)^2 \left(\frac{20\%}{\Pi_L} \right)^2. \quad (48)$$

The 68% confidence contour of measured polarization angle corresponding to $\Delta a_{1\sigma}$ is (Weisskopf et al. 2010)

$$\tan \chi_{1\sigma} = \frac{a_0 \sin \chi_0 + \Delta a_{1\sigma} \sin \psi}{a_0 \cos \chi_0 + \Delta a_{1\sigma} \cos \psi}, \quad (49)$$

where χ and χ_0 are the measured and true polarization angle (eq. [41]), respectively, and ψ is a free parameter. Finding the extrema of equation (49) yields $\psi_{\text{ext}} = \chi_0 \pm \arccos(-\Delta a_{1\sigma}/a_0)$. Setting $\chi_0 = 0$, to which the extrema of equation (49) are weakly sensitive, and keeping terms linear in $\Delta a_{1\sigma}/a_0$ yields

$$\Delta \chi_{1\sigma} = \chi - \chi_0 = \arctan \left(\frac{\Delta a_{1\sigma}}{a_0} \right) \simeq \frac{\Delta a_{1\sigma}}{a_0}. \quad (50)$$

One can then straightforwardly obtain the number of counts required for a given uncertainty in the polarization angle measurement

$$N_\chi = 1.5 \times 10^4 \left(\frac{10 \text{ deg}}{\Delta \chi_{1\sigma}} \right)^2 \left(\frac{0.5}{m} \right)^2 \left(\frac{20\%}{\Pi_L} \right)^2. \quad (51)$$

In this simple analysis, the ratio $N_\chi/N_\Pi \propto (n_\sigma/\Delta \chi)^2$ is insensitive to the modulation of the detector and the polarization fraction of the source.

For a given magnetar candidate, the count rate in a given energy band is

$$\dot{N}_{E_1-E_2} = \int_{E_1}^{E_2} \left(\frac{dN}{dE} \right) A_{\text{eff}}(E) dE, \quad (52)$$

where $[E_1, E_2]$ are the limits of the energy band, dN/dE the photon number flux, and A_{eff} is the effective area of GEMS. We obtain dN/dE from published fits to a handful of bright magnetar candidates in the sample of Kaspi & Boydstun (2010), which are selected to be in the quiescent stage¹⁴. It

¹⁴ We reconstruct the number flux dN/dE using the published fit parameters in XSPEC for the best-fit blackbody plus power law models with neutral absorption (PHABS) included. In cases where model normalizations were not reported, we chose values to match the reported (energy band integrated) fluxes or flux ratios. Since these models provide a reasonable fit for all sources under consideration here, they are sufficient for our approximate estimates.

TABLE 2
ESTIMATED GEMS COUNT RATES AND OBSERVATIONAL TIMES FOR SELECTED MAGNETAR CANDIDATES

| Object | \dot{N}_{2-10} (s ⁻¹) | \dot{N}_{2-4} (s ⁻¹) | \dot{N}_{4-10} (s ⁻¹) | T_{4-10}^{Π} (ks) | T_{4-10}^{χ} (ks) | Ref. ^a |
|-----------------------|-------------------------------------|------------------------------------|-------------------------------------|-----------------------|------------------------|-------------------|
| 4U 0142+61 | 3.27 | 3.12 | 0.15 | 27 | 101 | 1 |
| 1RXS J170849.0-400910 | 0.767 | 0.684 | 0.083 | 48 | 180 | 2 |
| 1E 1841-045 | 0.557 | 0.475 | 0.082 | 49 | 184 | 3 |
| 1E 2259+586 | 0.723 | 0.700 | 0.023 | 174 | 653 | 4 |
| SGR 1900+14 | 0.113 | 0.095 | 0.018 | 222 | 833 | 5 |

^aReferences: (1) White et al. (1996), (2) Rea et al. (2007b), (3) Morii et al. (2003), (4) Woods et al. (2004), (5) Mereghetti et al. (2006)

is well known that some of these sources experience long term changes in their flux and spectral properties (e.g., Kaspi 2007), hence these estimates serve as a rough reference rather than a detailed prediction.

The resulting count rates in photons per second are shown in Table 2. Alongside the number of counts over the entire sensitivity range of GEMS (2–10 keV), we show the rates over the soft and hard bands employed in §4.2 (2–4 keV and 4–10 keV, respectively), which contain the transition between thermal and non-thermal components, and the pure power-law regime in most sources, respectively. We also show fiducial integration times for the 4–10 keV frequency band,

$$T_{4-10}^{\Pi} = \frac{N_{\Pi}}{\dot{N}_{4-10}} \quad (53)$$

$$T_{4-10}^{\chi} = \frac{N_{\chi}}{\dot{N}_{4-10}}, \quad (54)$$

with $m = 0.5$, $\Pi = 20\%$, $n_{\sigma} = 3$ and $\Delta\chi_{1\sigma} = 10$ deg. Scaling the numbers with respect to this choice of parameters is straightforward.

Obtaining just one phase-averaged data point in the pure power-law region of the spectrum requires integration times of the order of tens of kiloseconds or more. Because the ratio of count rates in the 2–4 keV to 4–10 keV bands is 5–30, one would be guaranteed a higher energy resolution below 4 keV, unless the seed photons are very unpolarized. Even then, one would be able to detect a single data point with a 4.4% polarization fraction at 3- σ in the band 2–4 keV for 4U 0142+61. An unpolarized source of seed photons would require a cancellation of the contribution from returning currents and deep cooling (§2.2), which we consider to be a less likely scenario. Thus prospects for obtaining independent clues about the mechanism producing the non-thermal X-rays are certainly feasible for several of the brightest AXPs and SGRs.

The observational requirements for phase-resolved polarimetry, on the other hand, increase linearly with the number of data points per rotation period, if the same accuracy wants to be maintained. Measurement of the polarization fraction with 5 points in phase is not very demanding, at least for the brightest objects in Table 2. The 1 σ uncertainty in the polarization angle using T_{4-10}^{Π} per phase point is $\Delta\chi_{1\sigma} \simeq 20$ degrees, which is satisfactory if the spatial scale of the twist is large and the orientation is favorable (e.g., Figures 10, 13, and 15). Accurately capturing smaller variations in polarization angle in both spatial scale and amplitude (e.g., lowest panel in Figure 12), would become much more demanding, with count rates easily exceeding 10⁶ s even for 4U 0142+61.

A measure of the polarization angle would be especially useful around outbursts, as it has already been seen that sources experience persistent changes in torque and pulse profiles (e.g., Woods et al. 2004, 2007). Simultaneous monitoring with RXTE and high resolution spectra with Chandra or XMM-Newton would be the ideal complement to deep polarization observations.

6. SUMMARY AND DISCUSSION

We have studied the effects of resonant cyclotron scattering in a twisted magnetosphere on the outgoing polarization signal of magnetars. We have employed simple prescriptions for the magnetic field geometry, particle energy distribution, and seed spectrum. When the pair multiplicity is not too large, the dielectric properties of the magnetosphere are dominated by vacuum polarization out to large distances (eq. [17]), with the following implications:

1. – There is an effective separation of the regions where resonant cyclotron scattering and polarization eigenmode coupling take place, with the consequence that scattering occurs mostly in the adiabatic limit (Fig. 2). Because the light cylinder is safely outside of the zone where polarization modes freeze, circular polarization is always less than $\sim 10\%$ (e.g., Figure 4).
2. – Regardless of the polarization distribution of surface photons, resonant cyclotron scattering by transrelativistic charges introduces a characteristic polarization fraction of the order of ~ 10 –30%. This number arises from the mode exchange probability, dependence of optical depth on polarization, multiple scattering, and geometry of the system (§4.1). The transition from surface-dominated polarization to scattering-dominated takes place over a region of the spectrum extending over the interval ~ 2 –5 keV for a thermal spectrum with $kT = 0.4$ keV (Figures 17–20). Measurement of phase-averaged polarization fraction allows an unambiguous identification of resonant comptonization as the mechanism producing the non-thermal soft X-ray emission. This is particularly relevant for sources such as XTE J1810-197, whose spectrum can be fit with a comptonized model or two-temperature blackbody (Halpern & Gotthelf 2005).
3. Phase averaged measurements can also discern the dominant polarization mode of seed photons (Fig. 19), allowing an independent constraint on the mechanism providing the thermal luminosity. A dominance of E-mode photons in the thermal spectrum would favor deep cooling of the neutron star (Thompson & Duncan 1996), setting constraints on

magnetized atmosphere models (e.g., van Adelsberg & Lai 2006). An O-mode dominance in the unscattered component would indicate thermal emission from returning currents hitting the stellar surface (Thompson et al. 2002).

4. – Measurement of the phase-resolved polarization angle allows measurement of the spatial extent of the twist angle at radii $\sim 100R_{\text{NS}}$. Because the mode exchange probability always favors the E-mode regardless of system parameters (eq. [16]), scattered photons are predominantly in this linear eigenstate and their adiabatic propagation keeps track of the magnetic field geometry, with little sensitivity to input parameters. Photons remain mostly linearly polarized as eigenmodes couple, a direct consequence of the dominance of vacuum polarization and the slow rotation of magnetars. For each photon, the polarization vector preserves its orientation relative to the direction of the magnetic field at the point of freezing. In the case of a globally twisted dipole, it may even be possible to obtain the geometric parameters of the system by inverting the polarization angle as a function of phase. We have not explored this possibility (e.g., lower panels of Figures 10 and 14). It is worth keeping in mind that this effect is dependent on magnetospheric scattering only in that a particular eigenmode is preferred: in principle it is also present in the unscattered component (e.g., Heyl & Shaviv 2000).

5. – The asymmetries in the angular distribution of scattered radiation are due to the combination of charge motion along field lines and relativistic aberration. This also imparts an asymmetry in the polarization fraction. If scattering charges consist predominantly of electrons moving from one magnetic pole to the other, then a north-south asymmetry is introduced in the polarization fraction. Phase-resolved polarization fraction will display a peak displaced by one-half of a phase relative to the peak in intensity if the particle energy distribution is uni-directional (Figure 12). If the magnetosphere is dominated by pairs at these radii ($\sim 10R_{\text{NS}}$), then two symmetric peaks are expected in both the polarization distribution and the radiation flux, barring a strong asymmetry in the surface emission.

6. – Based on the expected sensitivity of GEMS and the spectra of a few bright magnetars, we estimate that phase-averaged polarimetry requires several tens to a few hundred kilosecond exposures per source for obtaining at least one data point in the non-thermal tail of the spectrum (Table 2). Phase-resolved polarimetry increases the requirements proportional to the number of points in phase for fixed accuracy. Detailed measurements of changes in the polarization angle as a function of phase seem feasible only for the brightest sources, and would require integration times approaching or exceeding a 10^6 s.

Our analysis ignores the contribution of the magnetospheric plasma to the dielectric tensor. This is a good approximation if the density of charge carriers satisfies $n_e \sim J/(ec)$, as found in Beloborodov & Thompson (2007). That study, however, focused on the inner part of the closed magnetosphere at radii $r \sim R_{\text{NS}}$, where a number of effects present at larger radii are absent. Pair cascades in the closed field circuit could be triggered by energy deposition from current driven instabilities close to the star (Thompson 2008a). A significant number of pairs at $\sim 100R_{\text{NS}}$ then alters the relative contribu-

tion of plasma and vacuum to the dielectric tensor (eq. [17]). When the plasma component is non-negligible, and $\omega \gg \omega_c$, propagation eigenmodes become increasingly circular as the charge density is increased, for most propagation directions (e.g., Mészáros 1992). Capturing this effect, particularly if the transition from vacuum to plasma dominated modes occurs around r_{pl} , requires a more careful consideration of the distribution of currents in the magnetosphere than our simple space-independent particle energy distribution. We have opted for a self-consistent (but potentially incomplete) first step in modeling this problem.

We have also ignored the contribution of scattering by ions close to the star (e.g., Thompson et al. 2002). Since the dielectric properties of the plasma would not change relative to the case analyzed here, we expect only quantitative changes relative to scattering by uni-directional electrons. Ion scattering would still be in the adiabatic limit, and modes would freeze at the same distance from the star as in the case of photons scattered by electrons. Hence, we would not expect significant changes in the phase dependence of the polarization angle. Changes would mostly affect the intensity and polarization fraction, and would be due to general relativistic effects (in photon propagation and magnetic field, the second of which we are ignoring) as well as due to reflection or absorption by the star, whose radius would now be comparable to the resonant surface. And obviously photons that escape the ion resonance surface can still be subject to scattering by electrons at larger radii, so the net observed anisotropies could increase.

Most of our calculations assume the simplest possible prescription for the seed photons: a blackbody of uniform surface temperature, 100% polarized, and isotropically emitting, in order to isolate the magnetospheric imprint on the polarization signal. Out of these assumptions, we expect those concerning the surface temperature and beaming distribution to potentially alter our results once they are relaxed. To gauge the effects of a non-uniform surface temperature, we have explored the extreme case of narrow polar caps around one or both magnetic poles, motivated by results from thermal conduction calculations with a strong internal toroidal field (Pérez-Azorín et al. 2006). We find minor differences relative to the uniform surface temperature distribution unless one polar cap emits substantially more than the other (Figs. [16] and [20]). A radiation intensity that has a non-trivial distribution around the local magnetic field (e.g., van Adelsberg & Lai 2006) could also distort the signature due to the directionality of particles. We have not addressed this issue here, as it would require a realistic atmosphere for self-consistency.

Given our assumptions, the polarization angle is an almost perfect tracer of the magnetic field geometry at $\sim 100R_{\text{NS}}$ from the star. In this study we have employed a very simple field geometry, which is self-similar and thus having a local direction independent of radial distance from the star. In a more realistic magnetosphere, the twist angle is not necessarily global, and evolves both in time and space (Thompson et al. 2002; Beloborodov & Thompson 2007; Thompson 2008a; Beloborodov 2009). Measurements of the magnetospheric twist at large radii would be most useful during and following periods of burst activity, where the magnetosphere is expected to undergo a significant rearrangement, as shown by changes in the pulse profiles before and after outbursts (e.g., Woods et al. 2004, 2007). A pulse profile with strong asymmetries and small-scale structure, if associated with localized twists, should be concurrent with a phase-resolved

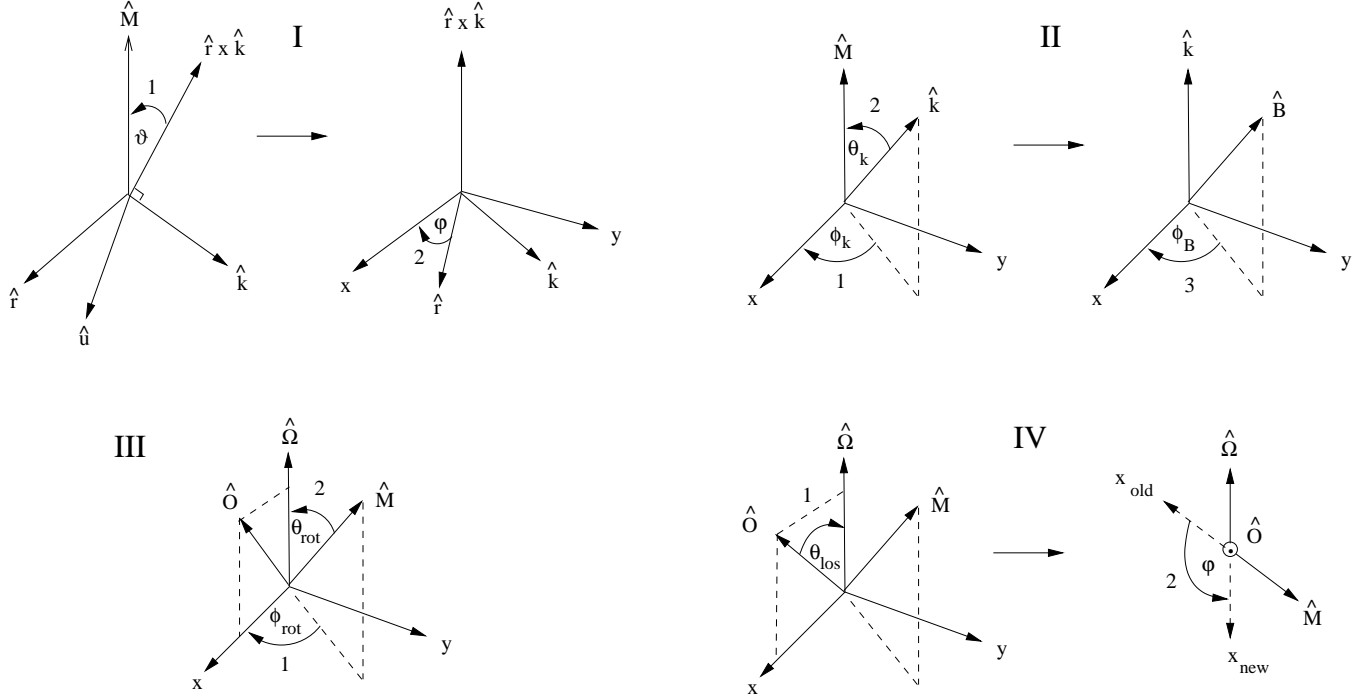


FIG. A1.— Coordinate systems and geometric transformations employed in the Monte Carlo calculation, labeled by roman numbers. The vectors \hat{M} , $\hat{\Omega}$, and \hat{O} denote the magnetic axis, rotation axis, and line-of-sight (see also eqns. [42] and [43]). The arabic numerals indicate the order in which each rotation matrix is applied (see text).

polarization angle that displays high temporal frequency and small amplitude components.

We thank Chris Thompson for stimulating discussions and comments on the manuscript. We also thank Tim Kallman and the GEMS team for providing instrument sensitivity data. Comments by an anonymous referee improved the presentation of the paper. R. F. is supported by NASA through

Einstein Postdoctoral Fellowship grant number PF-00062, awarded by the Chandra X-ray Center, which is operated by the Smithsonian Astrophysical Observatory for NASA under contract NAS8-03060. S. W. D. is supported by NSF AST-0807432, NASA NNX08AH24G, NSF AST-0807444, and in part by NSERC of Canada. Computations were performed at the IAS Aurora and CITA Sunnyvale clusters. The latter was funded by the Canada Foundation for Innovation.

APPENDIX

A. COORDINATE TRANSFORMATIONS

We present here all the coordinate transformations employed in the calculation. We denote the coordinate system with the magnetic axis \hat{M} in the z -direction by the subscript M . Each alternative coordinate system employed is labeled by roman number subscripts on vectors. Each of them is illustrated in Figure A1 and explained below. For conciseness, we write the transformations in terms of the elementary rotation matrices

$$R_x(\vartheta) = \begin{bmatrix} 1 & 0 & 0 \\ 0 & \cos \vartheta & -\sin \vartheta \\ 0 & \sin \vartheta & \cos \vartheta \end{bmatrix} \quad R_y(\vartheta) = \begin{bmatrix} \cos \vartheta & 0 & \sin \vartheta \\ 0 & 1 & 0 \\ -\sin \vartheta & 0 & \cos \vartheta \end{bmatrix} \quad R_z(\vartheta) = \begin{bmatrix} \cos \vartheta & -\sin \vartheta & 0 \\ \sin \vartheta & \cos \vartheta & 0 \\ 0 & 0 & 1 \end{bmatrix}, \quad (\text{A1})$$

which when applied to a column vector \mathbf{x} produce a counterclockwise rotation by an angle ϑ around each of the cartesian coordinate axes, respectively. We also make use of the more general angle-axis formula: given a unit vector \hat{u} , the rotation matrix that produces a counterclockwise rotation by an angle ϑ around $\hat{u} = u_x \hat{x} + u_y \hat{y} + u_z \hat{z}$ is

$$R_u(\vartheta) = \begin{bmatrix} u_x^2 + (1 - u_x^2) \cos \vartheta & u_x u_y (1 - \cos \vartheta) - u_z \sin \vartheta & u_x u_z (1 - \cos \vartheta) + u_y \sin \vartheta \\ u_x u_y (1 - \cos \vartheta) + u_z \sin \vartheta & u_y^2 + (1 - u_y^2) \cos \vartheta & u_y u_z (1 - \cos \vartheta) - u_x \sin \vartheta \\ u_x u_z (1 - \cos \vartheta) - u_y \sin \vartheta & u_y u_z (1 - \cos \vartheta) + u_x \sin \vartheta & u_z^2 + (1 - u_z^2) \cos \vartheta \end{bmatrix}, \quad (\text{A2})$$

with (A1) corresponding to $\hat{u} = \hat{x}$, \hat{y} , and \hat{z} , respectively.

A.1. Light Bending (I)

Since a photon orbit in a Schwarzschild metric has two conserved quantities (energy and angular momentum), one can map it to the $\theta = \pi/2$ plane in spherical polar coordinates without loss of generality (e.g., Schutz 2009). We choose the x -axis to be coincident with the position vector \hat{r} , and the \hat{z} axis along $\hat{r} \times \hat{k}$. The photon wave vector is transformed according to

$$\hat{k}_I = R_z(-\varphi) R_u(\vartheta) \hat{k}_M. \quad (\text{A3})$$

The first rotation around $\hat{u} = (\hat{r} \times \hat{k}) \times \hat{M} / |\hat{r} \times \hat{k}|$, with $\cos \vartheta = (\hat{r} \times \hat{k}) \cdot \hat{M} / |\hat{r} \times \hat{k}|$, puts the trajectory on to the equatorial plane. We then rotate the radial vector \hat{r} towards \hat{x} , with

$$\tan \varphi = \frac{[R_u(\vartheta)\hat{r}_M]_y}{[R_u(\vartheta)\hat{r}_M]_x}. \quad (\text{A4})$$

The normalized wave vector evolved in equations (29)-(32) corresponds to the components of \hat{k}_I in spherical polar coordinates. The transformation is ill-defined for radial propagation, which is nonetheless unaffected by light bending. In practice, we revert to planar propagation whenever $1 - |\hat{k} \cdot \hat{r}| < 10^{-6}$.

A.2. Polarization Evolution (II)

We start each integration of equations (21)-(22) in a frame such that the wave vector \hat{k} points in the z direction and the magnetic field lies in the $x-z$ plane. The transformation for the electric field vector \mathbf{A} is

$$\mathbf{A}_{II} = R_z(-\phi_B) R_y(-\theta_k) R_z(-\phi_k) \mathbf{A}_M, \quad (\text{A5})$$

where θ_k and ϕ_k are the polar and azimuthal angle of the wave vector relative to the magnetic axis, and

$$\tan \phi_B = \frac{[R_y(-\theta_k) R_z(-\phi_k) \hat{B}]_y}{[R_y(-\theta_k) R_z(-\phi_k) \hat{B}]_x}. \quad (\text{A6})$$

A.3. Rotational Phase (III)

Our coordinate system for phase-dependent quantities is such that the rotational axis $\hat{\Omega}$ points in the z -direction, and at phase zero both the magnetic axis \hat{M} and the direction to the line-of-sight \hat{O} are in the $x-z$ plane, at angles θ_{rot} and θ_{los} from $\hat{\Omega}$, respectively. What is needed are the coordinates of the line-of-sight \hat{O} relative to the magnetic axis, so that stored quantities are retrieved to construct phase curves. The transformation is

$$\hat{O}_M = R_y(-\theta_{\text{rot}}) R_z(-\phi_{\text{rot}}) \hat{O}_{III}, \quad (\text{A7})$$

with $\hat{O}_{III} = \sin \theta_{\text{los}} \hat{x}_{III} + \cos \theta_{\text{los}} \hat{z}_{III}$, and ϕ_{rot} the rotational phase.

A.4. Stokes Parameters (IV)

A rotation of the polarization plane around the wave vector affects only Q and U (Chandrasekhar 1960). Counterclockwise rotation by an angle φ yields

$$Q' = Q \cos 2\varphi + U \sin 2\varphi \quad (\text{A8})$$

$$U' = -Q \sin 2\varphi + U \cos 2\varphi. \quad (\text{A9})$$

For storage after photon escape to infinity, we take the x axis in the $\hat{k}-\hat{M}$ plane. For phase dependent quantities, however we rotate this axis to coincide with the $\hat{k}-\hat{\Omega}$ plane. The needed angle φ is obtained by rotating \hat{O}_{III} so that it lies along the \hat{z} axis, and then computing the azimuthal angle between $-\hat{M}_{IV}$ and $-\hat{\Omega}_{IV}$, thus

$$\tan(\pi - \varphi) = \frac{[R_y(-\theta_{\text{los}}) \hat{M}_{III}]_y}{[R_y(-\theta_{\text{los}}) \hat{M}_{III}]_x}, \quad (\text{A10})$$

where $\hat{M}_{III} = R_z(\phi_{\text{rot}}) R_y(\theta_{\text{rot}}) \hat{z}$ (eq. [A7]).

REFERENCES

- Adler, S. L. 1971, *Ann. Phys.*, 67, 599
 Albano, A., Turolla, R., Israel, G. L., Zane, S., Nobili, L., & Stella, L. 2010, *ApJ*, 722, 788
 Beloborodov, A. M. 2002, *ApJ*, 566, L85
 —. 2009, *ApJ*, 703, 1044
 Beloborodov, A. M., & Thompson, C. 2007, *ApJ*, 657, 967
 Black, J. K., Baker, R. G., Deines-Jones, P., Hill, J. E., & Jahoda, K. 2007, *Nuc. Inst. & Meth. Phys. Res. A*, 581, 755
 Chandrasekhar, S. 1960, *Radiative Transfer*, 1st edn. (New York: Dover)
 Costa, E., Soffitta, P., Bellazzini, R., Brez, A., Lumb, N., & Spandre, G. 2001, *Nature*, 411, 662
 Duncan, R. C., & Thompson, C. 1992, *ApJ*, 392, L9
 Fernández, R., & Thompson, C. 2007, *ApJ*, 660, 615
 Geppert, U., Küker, M., & Page, D. 2006, *A&A*, 457, 937
 Goldreich, P., & Julian, W. H. 1969, *ApJ*, 157, 869
 Güver, T., Özel, F., & Göğüş, E. 2008, *ApJ*, 675, 1499
 Güver, T., Özel, F., Göğüş, E., & Kouveliotou, C. 2007, *ApJ*, 667, L73
 Halpern, J. P., & Gotthelf, E. V. 2005, *ApJ*, 618, 874
 Heyl, J. S., & Hernquist, L. 1997, *J. Phys. A*, 30, 6485
 Heyl, J. S., & Shaviv, N. J. 2000, *MNRAS*, 311, 555
 Heyl, J. S., Shaviv, N. J., & Lloyd, D. 2003, *MNRAS*, 342, 134
 Kaspi, V. M. 2007, *ApSS*, 308, 1
 Kaspi, V. M., & Boydston, K. 2010, *ApJ*, 710, L115
 Klein, J. J., & Nigam, B. P. 1964, *Phys. Rev.*, 135, 1279
 Lai, D., & Ho, W. C. 2003a, *PRL*, 91, 71101
 Lai, D., & Ho, W. C. G. 2002, *ApJ*, 566, 373
 —. 2003b, *ApJ*, 588, 962
 Lyutikov, M., & Gavril, F. P. 2006, *MNRAS*, 368, 690
 Mereghetti, S., Esposito, P., & Tiengo, A. 2007, *ApSS*, 308, 13
 Mereghetti, S., et al. 2006, *ApJ*, 653, 1423
 Mészáros, P. 1992, *High-Energy Radiation from Magnetized Neutron Stars*, 1st edn. (Chicago: Univ. of Chicago Press)
 Morii, M., Sato, R., Kataoka, J., & Kawai, N. 2003, *PASJ*, 55, L45
 Nobili, L., Turolla, R., & Zane, S. 2008, *MNRAS*, 386, 1527
 Novick, R., Weisskopf, M. C., Berthelsdorf, R., Linke, R., & Wolff, R. S. 1972, *ApJ*, 174, L1
 Pavan, L., Turolla, R., Zane, S., & Nobili, L. 2009, *MNRAS*, 395, 753
 Pavlov, G. G., & Zavlin, V. E. 2000, *ApJ*, 529, 1011
 Pérez-Azorín, J. F., Miralles, J. A., & Pons, J. A. 2006, *A&A*, 451, 1009

- Rea, N., Turolla, R., Zane, S., Tramacere, A., Stella, L., Israel, G. L., & Campana, R. 2007a, *ApJ*, 661, L65
- Rea, N., Zane, S., Turolla, R., Lyutikov, M., & Götz, D. 2008, *ApJ*, 686, 1245
- Rea, N., et al. 2007b, *ApSS*, 308, 505
- Rybicki, G. B., & Lightman, A. P. 2004, *Radiative Processes in Astrophysics*, 2nd edn. (Weinheim: WILEY-VCH)
- Schutz, B. 2009, *A First Course in General Relativity*, 2nd edn. (Cambridge: Cambridge Univ. Press)
- Swank, J., Kallman, T., Jahoda, K., Black, K., Deines-Jones, P., & Kaaret, P. 2010, in *X-ray Polarimetry: A New Window in Astrophysics*, ed. R. Bellazzini, E. Costa, G. Matt, & P. Tagliaferri (Cambridge: Cambridge Univ. Press), 251
- Thompson, C. 2008a, *ApJ*, 688, 1258
- . 2008b, *ApJ*, 688, 499
- Thompson, C., & Duncan, R. C. 1995, *MNRAS*, 275, 255
- . 1996, *ApJ*, 473, 322
- Thompson, C., & Duncan, R. C. 2001, *ApJ*, 561, 980
- Thompson, C., Lyutikov, M., & Kulkarni, S. R. 2002, *ApJ*, 574, 332
- van Adelsberg, M., & Lai, D. 2006, *MNRAS*, 373, 1495
- van Adelsberg, M., & Perna, R. 2009, *MNRAS*, 399, 1523
- Wang, C., & Lai, D. 2007, *MNRAS*, 377, 1095
- . 2009, *MNRAS*, 398, 515
- Weisskopf, M. C., Elsner, R. F., & O'Dell, S. L. 2010, in *Space Telescopes and Instrumentation 2010: Ultraviolet to Gamma Ray*, ed. M. Arnaud, S. S. Murray, & T. Takahashi (SPIE Digital Library: SPIE), 77320E–1
- White, N. E., Angelini, L., Ebisawa, K., Tanaka, Y., & Ghosh, P. 1996, *ApJ*, 463, L83
- Woods, P. M., Kouveliotou, C., Finger, M. H., Göğüş, E., Wilson, C. A., Patel, S. K., Hurley, K., & Swank, J. H. 2007, *ApJ*, 654, 470
- Woods, P. M., & Thompson, C. 2006, in *Compact stellar X-ray sources*, ed. Lewin, W. H. G. & van der Klis, M. (Cambridge: Cambridge Univ. Press), 547–586
- Woods, P. M., et al. 2004, *ApJ*, 605, 378
- Zane, S., Rea, N., Turolla, R., & Nobili, L. 2009, *MNRAS*, 398, 1403
- Zheleznyakov, V. V. 1996, *Radiation in Astrophysical Plasmas*, 1st edn. (Dordrecht: Kluwer)